Niraula, Abinab; Remes, Heikki; Nussbaumer, Alain

Strain-based analysis on the influence of local undercut geometry on fatigue crack initiation life

Published in:
International Journal of Fatigue

DOI:
10.1016/j.ijfatigue.2024.108392

Published: 01/09/2024

Document Version
Publisher's PDF, also known as Version of record

International Journal of Fatigue 186 (2024) 108392

Contents lists available at ScienceDirect

International Journal of Fatigue

journal homepage: www.elsevier.com/locate/ijfatigue

Strain-based analysis on the influence of local undercut geometry on fatigue crack initiation life

Abinab Niraula [a,b,*], Heikki Remes [a], Alain Nussbaumer [c]

[a] Aalto University, School of Engineering, Department of Mechanical Engineering, P.O. BOX 14100, FI-00076 AALTO, Finland
[b] Meyer Turku Oy, Turku FI-20240, Finland
[c] EPFL, Institute of Civil Engineering, RESSLab, 1015 Lausanne, Switzerland

ARTICLE INFO

Keywords:
Fatigue
Strain-based analysis
Undercut
3D geometry
Local weld notch

ABSTRACT

The local undercut defects at the weld toe provide a potential initiation site for fatigue cracks and significantly impact the structure's fatigue strength. The influence of continuous undercut depth on fatigue performance is widely studied, but the research on the influence of local undercut geometry is limited. In this research, the influence of the 3D undercut geometry on the fatigue strength of welded joints is investigated using the elasto-plastic finite element analysis, with explicit consideration of geometry and plasticity effect. A simplified parametric model is created to represent the realistic undercut geometry based on high-resolution measurement data. The combination of the geometric parameters for the realistic undercut models was filtered from a full-factorial design of six undercut geometry parameters. The influence of the individual geometric parameters of the local undercut defect such as depth, radius, width, and length on the fatigue performance of weld is systematically investigated. Based on the results, a three-dimensional undercut geometry index is proposed in the current study and found suitable for estimating fatigue crack initiation life. Furthermore, the research provides insights into fatigue strength-based quality criteria for welds with local undercut defects.

1. Introduction

Sustainable utilization of earthly resources demands highly optimized manufacturing methods in large-scale steel structures to provide high-performing lightweight structures. Shipbuilding is one of the industries where an enormous amount of steel is welded together to form the structural components of the ship. During the operational lifetime, the ship's structures are subjected to millions of load cycles, and thus, fatigue is one of the most important design factors. The welded components of ships are designed for high-cycle fatigue life, which is the sum of the fatigue crack initiation life and fatigue crack propagation life. The fatigue crack initiation life is the estimated number of fatigue load cycles to develop microstructurally short cracks (1–10 grains long) at the fatigue critical location. In the structures designed for high-cycle fatigue life, the total fatigue life is dominated by the fatigue crack initiation life [1] and geometric defects like undercuts that provide potential fatigue crack initiation sites in welded structures. Furthermore, weld defects such as undercuts significantly affect high-cycle fatigue and have a comparatively small effect on low-cycle fatigue [2]. Undercuts are inherent to fusion-based welding processes as they can form during the solidification of the molten weld pool, resulting in various shapes and sizes. Therefore, it is essential to understand the influence of undercut geometry on the fatigue crack initiation life of welded structures to achieve the goals of producing high-performing, lightweight, and sustainable welded structures for transportation and civil industries.

To ensure the strength and fatigue requirements of welded structures, the weld undergoes several quality inspections where the weld geometry and misalignments are monitored, and the weld defects are inspected. Generally, these approaches based on existing standards are sufficient for normal-quality welds. However, in the case of high-performing welds, the undercut defects are significantly smaller and more challenging to characterize [3]. The existing criteria to characterize the undercut defects are based on 2D profiles and assume continuous defects [4–7], whereas a significant number of local undercuts with different geometries were observed in recent research [3,8]. Furthermore, the allowable undercut depth limit of 0.5 mm in the current quality criterion was found to be detrimental for high-performing welds as this could not distinguish between welds with significantly different fatigue strengths [3]. Moreover, current quality criteria on the length of undercuts can only differentiate between

* Corresponding author at: Aalto University, School of Engineering, Department of Mechanical Engineering, P.O. BOX 14100, FI-00076 AALTO, Finland.
E-mail address: abinab.niraula@aalto.fi (A. Niraula).

https://doi.org/10.1016/j.ijfatigue.2024.108392
Received 20 March 2024; Received in revised form 10 May 2024; Accepted 12 May 2024
Available online 14 May 2024

continuous and intermittent undercuts [5,7,9], and no criteria exist for the 3D geometry characterization of undercuts despite the significant occurrences of local undercuts of different shapes and sizes. Current standards define the undercut defect with only the undercut depth (d), and most of the literature with the two parameters: undercut depth (d) and undercut radius (r). Although the ratio of undercut depth to undercut radius (d/r) has significance for continuous undercut [10–12], it omits the 3D geometry of non-continuous local undercut. Furthermore, the measurement of the radius has its challenges, as pointed out by several researchers [2,3,13,14], and can potentially lead to significant uncertainties if utilized for quality control purposes [3]. Additionally, the existing numerical studies on the geometry of the undercut utilizes idealized 2D geometry where the geometric parameters are individually varied, which has limited capability to describe the 3D undercut geometry. Such an approach overlooks the fact that the geometric parameters of an undercut are still co-dependent despite the lack of a clear statistical correlation, and a change in one of the parameters induces changes in other parameters.

The local undercut geometry is formed during the solidification of the weld pool in the welding process. With respect to the formation of local undercut geometry, it is worth noting that the flow of the weld pool is governed by the physical forces present in the weld pool and the external pressure of shielding gas [8,15,16], which influences the weld pool's solidification and hence the shape of the undercuts. The undercuts exhibit geometric continuity on a local scale as it is a consequence of the solidification process of the molten weld pool, and a change in one geometric parameter induces a change in other parameters. Despite closely related geometric parameters, no clear correlations between the undercut geometric parameters were found in the literature [2,17–19]. Nonetheless, previous experimental investigations of the undercut geometry show the trend of decreasing undercut radius with increasing undercut depth [3,19]. The investigations of the relation between the 3D geometric parameters of undercut and their combined influence on fatigue are lacking. The investigation on realistic 3D undercut geometry is limited in research not only because it is computationally highly demanding but also because the digital measurement methods have only recently been developed enough to enable field measurement of welds with high enough accuracy and resolution for the precise measurement of undercut geometry [3]. Recent research utilizing modern digital measurement methods has focused on weld geometry, such as weld size, weld flank angle, transition radius, and 2D undercut geometry parameters, but has mostly excluded the length dimension of undercut; see, e.g. [20–22].

The influence of individual undercut geometry parameters on the fatigue strength of welds has been studied with experimental and numerical methods in literature [17,23–28]. The significant influence of undercut depth on the stress concentration factor was demonstrated for welded joints with 2D weld simulations by various researchers [23–26,28]. Improvement of fatigue performance by increasing the width of the local undercut while maintaining depth and radius constant was demonstrated in previous research with 2D FEA [23,26]. The ratio of undercut depth to undercut radius has been investigated in theoretical studies [10–12], especially with fracture mechanics approaches where it has significance for crack propagation kinematics and fatigue strength. These studies indicate that stress concentration factors and fatigue strength can be better estimated with a combination of geometry parameters instead of individual undercut geometry parameters.

Significant improvement in the fatigue life estimation was shown when utilizing detailed 3D weld geometry scan data from the weld compared to an idealized geometry [29]. Liinalampi et al. investigated the 3D undercut geometry, taking the length of the undercut into account, and demonstrated that an undercut acts as a continuous undercut when the undercut length is at least ten times the undercut depth [30]. The research also showed that the fatigue-relevant stresses are overestimated in 2D analyses for deep notches with a short length, therefore highlighting the necessity of acknowledging the 3D undercut geometry for the analyses of local undercuts. Hence, the current paper investigates the influence of the shape and size of the local 3D undercuts on fatigue crack initiation life of high-performance welds, utilizing simplified parametric undercut geometry and cyclic elasto-plastic finite element analysis for explicit consideration of geometry and plasticity effects. The 3D undercut geometry of the current study is based on the experimental high-resolution measurements of undercut defects, measured with an accuracy of better than 1 μm. The current study utilizes the full factorial design to explore all possible combinations of the 3D geometric parameters to create realistic undercut geometries for numerical analyses. To reduce the computational costs, the geometric combinations are randomly resampled to create a well-distributed set of undercut shapes, ensuring full coverage of the geometric domain to include various undercut shapes and sizes. Numerical investigation is applied in the current study to facilitate the comprehensive coverage of geometric combinations and the potential interplay between the undercut parameters.

2. Characterization of undercut geometry

2.1. Geometry modeling of local undercut

Undercuts have complex geometries with irregular surfaces and cross-sectional profiles. Thus, modeling the exact geometry of the undercut requires a large number of high-accuracy measurement points to define the shape contours. This is technically demanding, practically challenging, and computationally time-consuming. Furthermore, the structural analysis of such detailed undercut geometry requires a very fine mesh, resulting in a large number of elements, which is computationally demanding. The undercut geometry needs to be simplified with a minimum number of geometric parameters to facilitate the sensitivity analysis of the undercut's shape and size on the welds' fatigue performance. This paper simplifies the undercut geometry found in welded joints [3,8,22,30] to generate realistic 3D undercut models based on the observations from high-resolution and high-accuracy weld measurements. A parametric 3D undercut model was created to generate realistic undercut geometries, enable sensitivity analysis of undercut geometry parameters, and explore the geometries beyond the limits of the measured values.

The undercut geometry in our experimental observations has been of symmetric and asymmetric types and is in line with observations from the literature; see [3,22,30]. The symmetric undercut has its deepest contour in the middle of its width and length, while the asymmetric undercut has the deepest point away from the middle of the undercut length, width, or both. Fig. 1 shows a schematic representation of symmetric and asymmetric undercut geometries and a cutout of an asymmetric 3D undercut model. The parametric 3D undercut geometry created for this research is capable of generating both symmetric and asymmetric undercuts. The geometry is created utilizing 2D control sections in the undercut width (w) and undercut length (l) direction, as shown in Fig. 2. The d, r, and w are controlled by the 2D section perpendicular to the weld direction, and the undercut length profile is

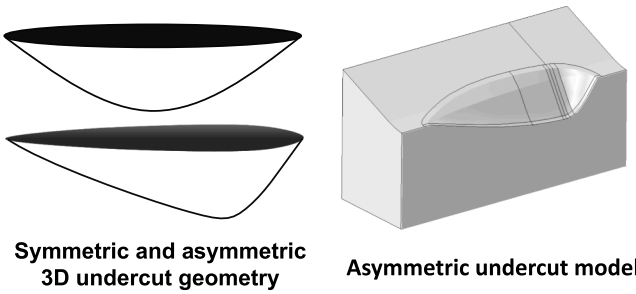

Fig. 1. Symmetric and asymmetric undercut geometry example.

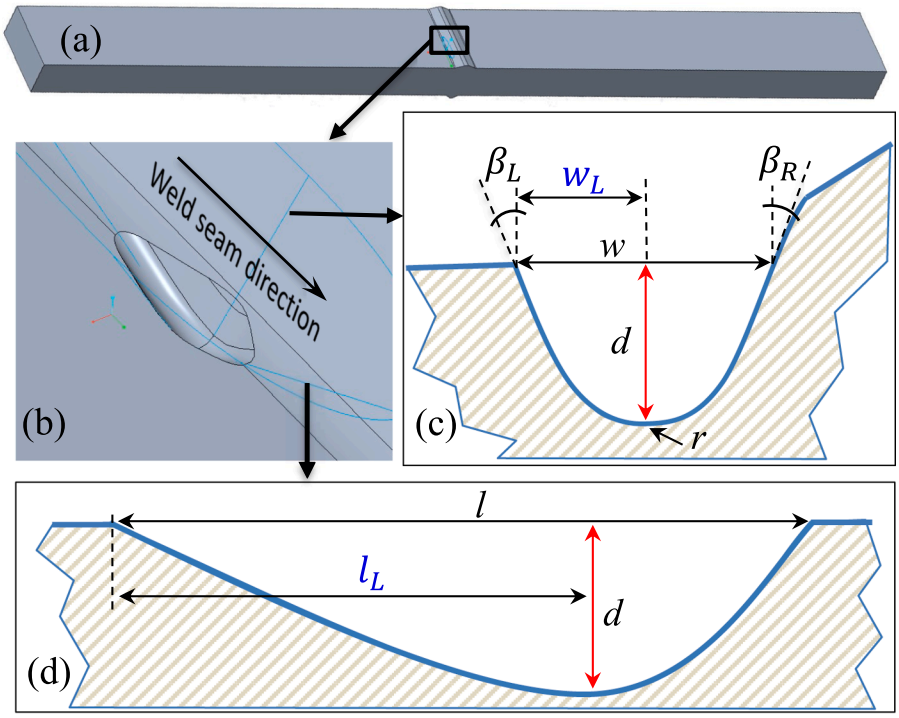

Fig. 2. Schematic diagram of 2D control curves for the undercut geometry. (a) specimen showing weld seam direction and location of undercut, (b) undercut location at the weld toe, (c) 2D control curve perpendicular to weld, and (d) parallel to the weld.

controlled by the 2D section parallel to the weld direction. The 2D profiles are constrained to have a zero slope at the deepest point of the undercut, and the surroundings are formed following the splines along all directions to form the Non-Uniform Rational B-Splines (NURBS) based surface of the undercut. The opening of the undercut is created at the top surface of the plate with four-quarters of ellipses with several geometry constraints enforced to make a smooth and continual geometric profile. In addition to d, r, l, and w, the left segment of undercut width (w_L) and left segment of undercut length (l_L) from the deepest undercut location are specified to describe asymmetric undercuts as shown in blue in Fig. 2c-d and 3c. These six parameters can fully define the 3D asymmetric and symmetric undercut geometry, as shown in Fig. 3 below. The asymmetry along the length (*asymL*) and width (*asymW*) of the undercut is defined with respect to the length and width of the undercut, as shown in equations (1) and (2). The total asymmetry (*asym*) is scaled to have values between 0 and 1 where symmetric undercut has value 0, and asymmetric is towards value 1, as defined in equation (3).

$$asymL = \left| \left(1 - \frac{2\,l_L}{l}\right) \right| \tag{1}$$

$$asymW = \left| \left(1 - \frac{2\,w_L}{w}\right) \right| \tag{2}$$

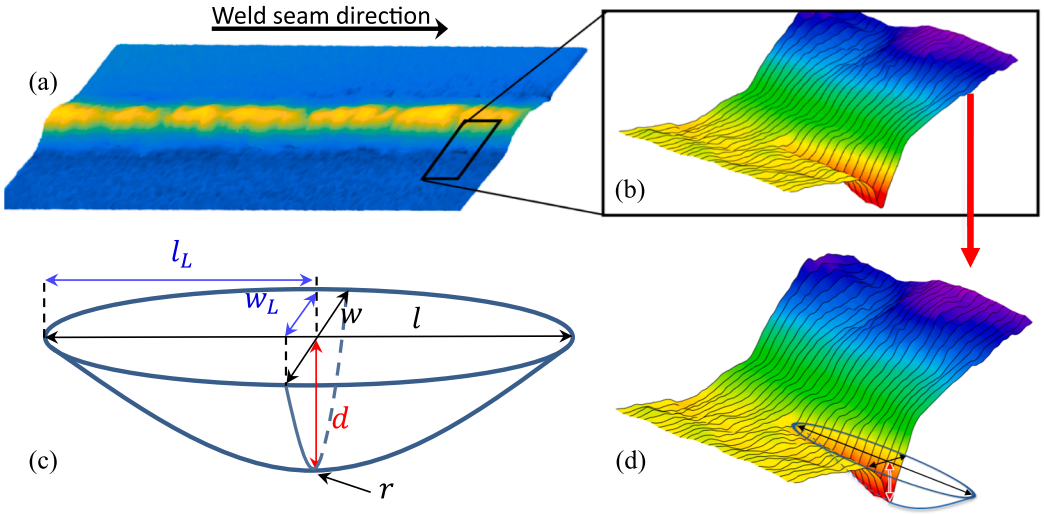

Fig. 3. (a-b) High-resolution 3D scan of weld seam showing an undercut defect [3], (c) schematic diagram of the undercut with the undercut geometry parameters, and (d) simplified and scanned undercut geometry.

$$asym = \sqrt{\frac{1}{2}\left[\left(1-\frac{2\,l_L}{l}\right)^2+\left(1-\frac{2\,w_L}{w}\right)^2\right]} \quad (3)$$

The undercut opening angle is not a control parameter in the current study but is measured from the resulting shape of the undercut during the geometry creation stage. The simplified undercut model is validated with elasto-plastic FEA of an observed undercut geometry (see Fig. 3b) and is presented in the results chapter. The validation case corresponds to a typical undercut in laser-hybrid welded butt joints. The measurement is done with FocalSpec Oy's LCI 1600 Sensor, similar to [3], which utilizes Line Confocal Imaging technology to scan and calculate the 3D location of the measurement point with an accuracy of better than 1 μm. The 3D measurement points from the scanned undercut geometry are utilized to fit NURBS-based surfaces with C^2 continuity for the undercut geometry to create the scanned undercut model. The six undercut geometry parameters measured from the scanned undercut are utilized in the parametric model to generate the simplified undercut model.

The simplification of the parametric undercut geometry assumes a skewed paraboloid shape made up of four-quarters of paraboloids to enable the modeling of asymmetric and symmetric undercuts. The shape is based on the experimental observation of undercut defects with high-resolution scans where a significant proportion of undercuts were asymmetric. The range of geometric parameters is based on measurements and the recent experimental study of undercut defects on laser-MAG hybrid welds [3]. The range of geometric parameters for the current investigation is further extended to explore different potential shapes and sizes of undercuts. Each parameter is assigned multiple values based on the defined step size, as illustrated in Table 1. The chosen undercut geometry and range of investigations are comparable to the undercuts presented in earlier studies [22,30], and the allowable undercut depth in existing standards for welds subjected to fatigue load [5].

2.2. Design of Experiment for geometric parameters

An undercut has a specific combination of the six geometric parameters presented in Table 1. In the absence of a relation among the undercut geometry parameters, the formulation of the 3D undercut geometry requires the explicit definition of each geometry parameter. However, they cannot be randomly assigned as they need to represent a realistic undercut shape. In the current paper, the geometric parameter combinations are designed with a multi-level full factorial Design of Experiment to explore all the potential shapes of the undercut, resulting in 2.5 million combinations. Geometric constraints were applied to filter out the unrealistic and physically impossible undercut shapes, and the undercuts to be modeled were randomly resampled from the resulting list of realistic geometric combinations. The geometric constraints applied to select realistic shapes are based on the observations in the measurements and the literature-based assumption that the local undercut surface is continuous and does not have sudden jumps on the local scale. The shape of the undercut is influenced by the weld pool and plasma flow during the welding and solidification process, which results in a continuous surface at the local undercut scale. Therefore, the undercut radius in the current study is limited to 80 % of the distance from the undercut depth center to the undercut wall. The geometric constraints applied to filter the undercut geometry combinations are listed below.

Table 1
Geometric parameters of undercut and their dimensional ranges in current investigation.

Undercut geometry parameters	Range of dimension	Step size
Depth (d)	100 – 500 μm	25 μm
Radius (r)	50 – 300 μm	20 μm
Width (w)	100 – 400 μm	50 μm
Left side width (w_L)	25 – 375 μm	25 μm
Length (l)	0.8 – 2.5 mm	200 μm
Left side length (l_L)	50 μm – 2 mm	200 μm

- Left or right segment of undercut width from the center of the undercut cannot be larger than undercut width: (w_L, ($w - w_L$)) $< w$
- Left or right segment of undercut length from the center of the undercut cannot be larger than undercut length: (l_L, ($l - l_L$)) $< l_L$
- Undercut radius (r) cannot be larger than 80 % of the smaller width segment from the center of undercut: (50 μm $< r <$ 80 % of min (w_L, ($w - w_L$))

No relations are assumed between the undercut geometry parameters in selecting geometry combinations, as long as they result in realistic undercuts. The investigated undercut shapes contain the geometric parameters throughout the full range of the dimensions from Table 1, as shown in the matrix plot in Fig. 4. It is worth noting that the distributions of geometric parameters in Fig. 4. are due to the random resampling and not the geometry constraints used in the filtering process. The geometric dimensions of the investigated undercuts are presented in Appendix A.

2.3. Undercut opening angle

An undercut has two flank angles on either side of the centerline, as shown in Fig. 2c and Fig. 5e. It is worth noting that the undercut flank angles are not control parameters for the undercut geometry creation in current research and are measured from the modeled undercut geometries to study their influence on fatigue. To reduce the number of geometric parameters, an undercut opening angle (β) was calculated by combining the two undercut flank angles (β_L and β_R) from the cross-section perpendicular to the weld direction at the deepest contour of each undercut model, as shown in Fig. 5e. The undercut opening angle decreases with an increase in d and a decrease in w, as shown in Fig. 5a-b. Furthermore, the ratio of d/w shows a significantly stronger relation to the undercut opening angle than the d/r ratio, as shown in Fig. 5c-d.

3. Finite element analysis

The 3D FE analyses of the undercut geometries are performed with the sub-modeling technique in two stages: a global model for the weld and plate geometry, and a local undercut sub-model for the undercut geometry. The global model considers the plate thickness, weld nominal geometry, and the position of the undercut in the weld. The height, width, flank angle, transition radius, and profile of the weld on both the top and bottom sides are defined in the global model, as shown in Fig. 6a. The weld dimensions are presented in Table 2 and represent the geometry of the laser-MAG welded butt joint with a characteristic fatigue strength of FAT100. The global model represents a 10 mm thick and 40 mm wide butt-welded plate of 250 mm length where the undercut is located at the centerline of the global model and parallel to the weld direction at the weld toe of the welding side as shown in Fig. 6b and 3b. It is worth noting that the position of the undercut along the weld seam is not expected to significantly affect the results of the current study, as the surrounding boundary conditions remain largely uniform. The position of undercut in current research is based on experimental observations where all significant undercuts were found by the weld toe at the junction of the weld flank and base plate. This observation is supported by the physical mechanism of undercut formation where the undercut forms at the transition zone between the weld pool and base plate [8,15,16]. The weld geometry and the plate thickness are kept constant to focus on the influence of the undercut geometry in the current study. The detailed geometry of the undercut is defined in the local sub-model stage with the six geometric parameters shown in Fig. 3c and listed in Table 1. The 3D displacement history of six load cycles from the nodes of global model corresponding to the outermost

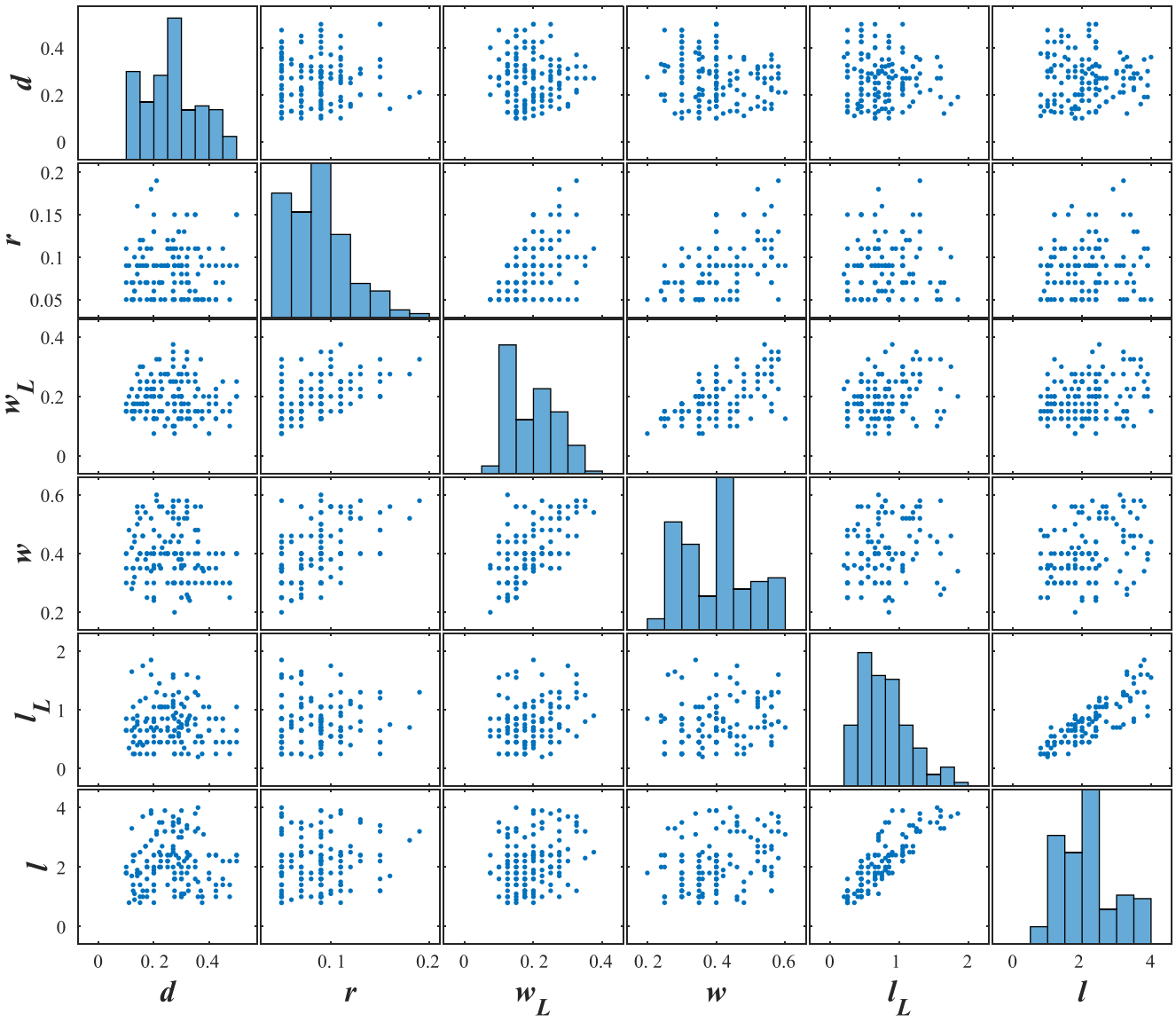

Fig. 4. Matrix plot to show the combinations of the six undercut geometry parameters to create the undercut models.

nodes of the local undercut sub-model is applied as the input load for the local undercut model. Fig. 6b-c shows the global model with the load and boundaries, the location of the undercut, and the local undercut model along with its mesh. The Voce-Chaboche material model is utilized on the global model, submodel and continuum-based single-element model (CSEM) for the elasto-plastic simulation of the undercut, which can model both isotropic and kinematic hardening of the material [31]. The material parameters for the Voce-Chaboche (VC) material model are adopted from [31], as shown in Table 3. An example of the resulting elasto-plastic material response from an element at the undercut depth is shown in Fig. 9.

The global model is fixed on one end and a cyclic tensile load is applied on the other end with a load ratio of R = 0, and a plate nominal stress range of 172 MPa corresponding to the high-cycle fatigue experiments in [3]. Furthermore, a selected set of undercut models was simulated with three different stress ranges of 150 MPa, 172 MPa, and 200 MPa to investigate the influence of varying load levels. Since the fatigue phenomena is a localized process, the fatigue-relevant stress for the fatigue crack initiation life estimation is averaged within material microstructure-dependent averaging distance and perpendicular to the maximum principal stress from the surface of the undercut, similar to [10,32]. The 10 μm averaging distance is used in the current study, corresponding to a 99 % probability grain size of laser-MAG hybrid weld [33]. The undercut FE model is meshed progressively starting from 2 μm sized brick elements (C3D8R) at the stress averaging unit with a linear shape function and a single integration point, resulting in FE models with 500 k to several million elements. The FE models are created to have at least four elements within the stress averaging unit with the smallest element size of 2 μm. Based on the convergence analysis, this mesh resulted in sufficient accuracy, i.e. a maximum of 2 % difference in stresses and strains. Fig. 6b-c shows the mesh of the undercut sub-model, and Fig. 7 shows the stress averaging path at the maximum principal stress location with the mesh around the stress averaging path. An elasto-plastic simulation of an undercut model with 1.35 million C3D8R and C3D6 elements took approximately 103 h on a local desktop workstation utilizing 16 cores of i7 CPU, 32 GB memory, and 8 GB dedicated professional NVIDIA GPU due to the computationally demanding nature of the FEA model. Therefore, the rest of the FEA was performed with ABAQUS 2022 solver utilizing Puhti supercomputer of CSC – IT Center for Science [34] with up to 480 CPUs and 2.4 TB memory for the largest models.

To calculate the fatigue-relevant stresses and strains, first the averaged stress is defined for an averaging volume unit of the undercut. Then, the strain amplitude (ε_a) for the fatigue crack initiation life is

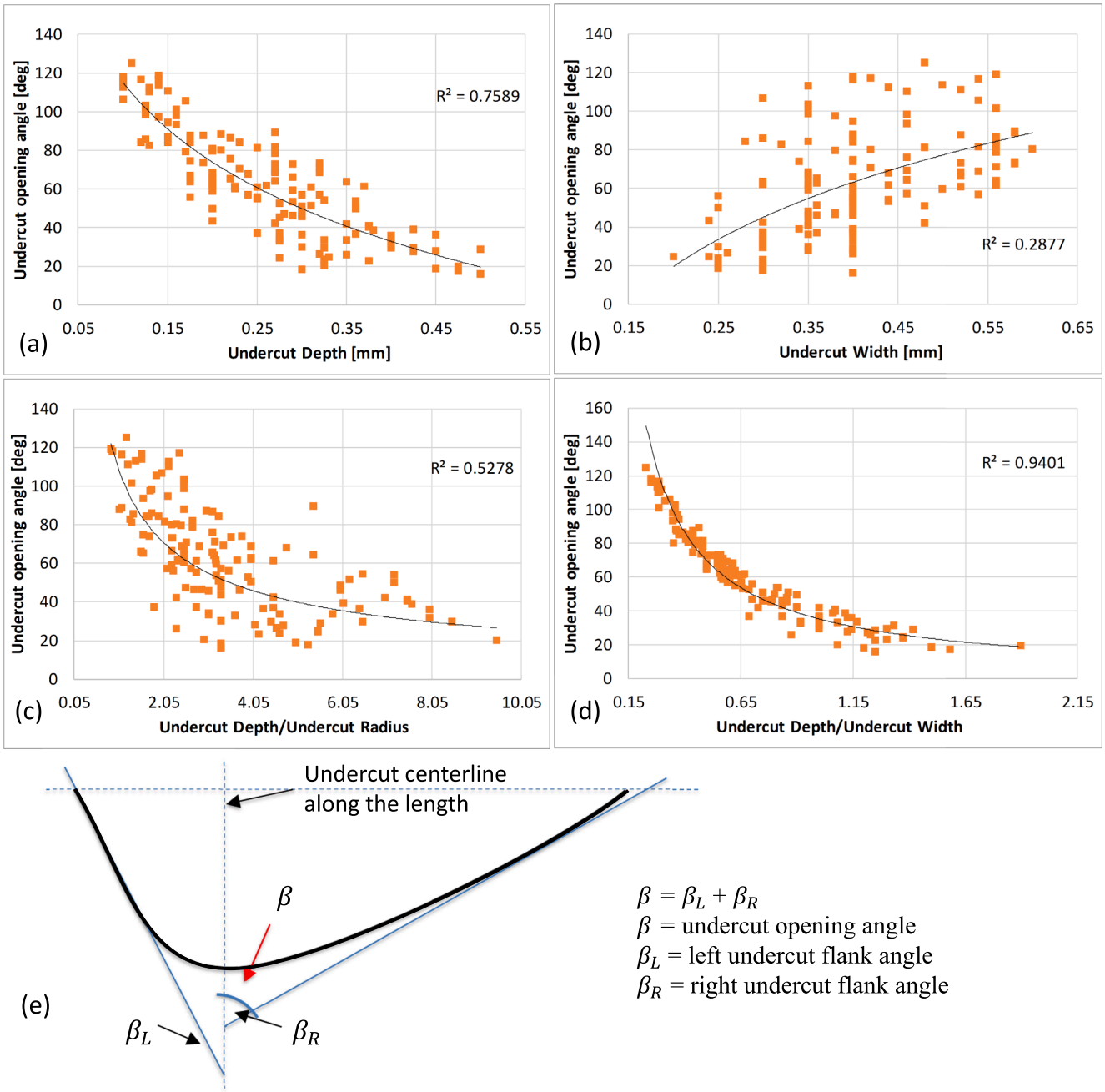

Fig. 5. The relation of undercut opening angle to: (a) undercut depth, (b) undercut width, (c) d/r, (d) d/w, and (e) schematic diagram of undercut opening angle.

calculated for the averaged stresses considering the material's elasto-plastic behavior utilizing a continuum-based single-element model (CSEM). Within this approach, the fatigue-effective stresses and strains follow the isotropic and kinematic hardening behavior based on the Voce-Chaboche (VC) material model [35]. In the CSEM, the history of principal stresses from the averaging unit is utilized as input load on a single element. The strain amplitude from the last load cycle of the CSEM is used to estimate the fatigue crack initiation life. Fig. 8a shows the CSEM load history extracted from the undercut sub-model. Fig. 8b-c shows the boundary conditions and the load applied on the CSEM. The strain amplitude is calculated as half of the strain range from the highest and lowest load points of the last stress cycle indicated by red and blue stars, respectively, in Fig. 8a.

The stress–strain response was stable after the first four cycles, and the difference in strain ranges after 6th cycle was minimal (<0.615 %). Therefore, FEA was run for six cycles on all undercut models, and the fatigue crack initiation life was estimated based on the 6th cycle results with the mean stress-corrected strain–life equation shown below. The fatigue strength coefficient σ_f' and ductility coefficient ε_f' of the strain-life equation are estimated based on average Brinell hardness (HB) tests [36]. The Smith-Watson-Topper fatigue damage criteria was calculated from the FEA results utilizing the averaged maximum principal stress (σ_{max}) and the strain amplitude (ε_a) (SWT parameter = $\sigma_{max}\varepsilon_a$), and the fatigue crack initiation life was calculated for each undercut model with equation (4):

$$\sigma_{max}\varepsilon_a = \frac{(\sigma_f')^2}{E}(2N_f)^{2b} + \sigma_f'\varepsilon_f'(2N_f)^{b+c} \tag{4}$$

where $\sigma_f' = 1125.74, \varepsilon_f' = 0.496, b = -0.09,$ and $c = -0.56$. The parameters b and c are fatigue strength and ductility coefficient exponents.

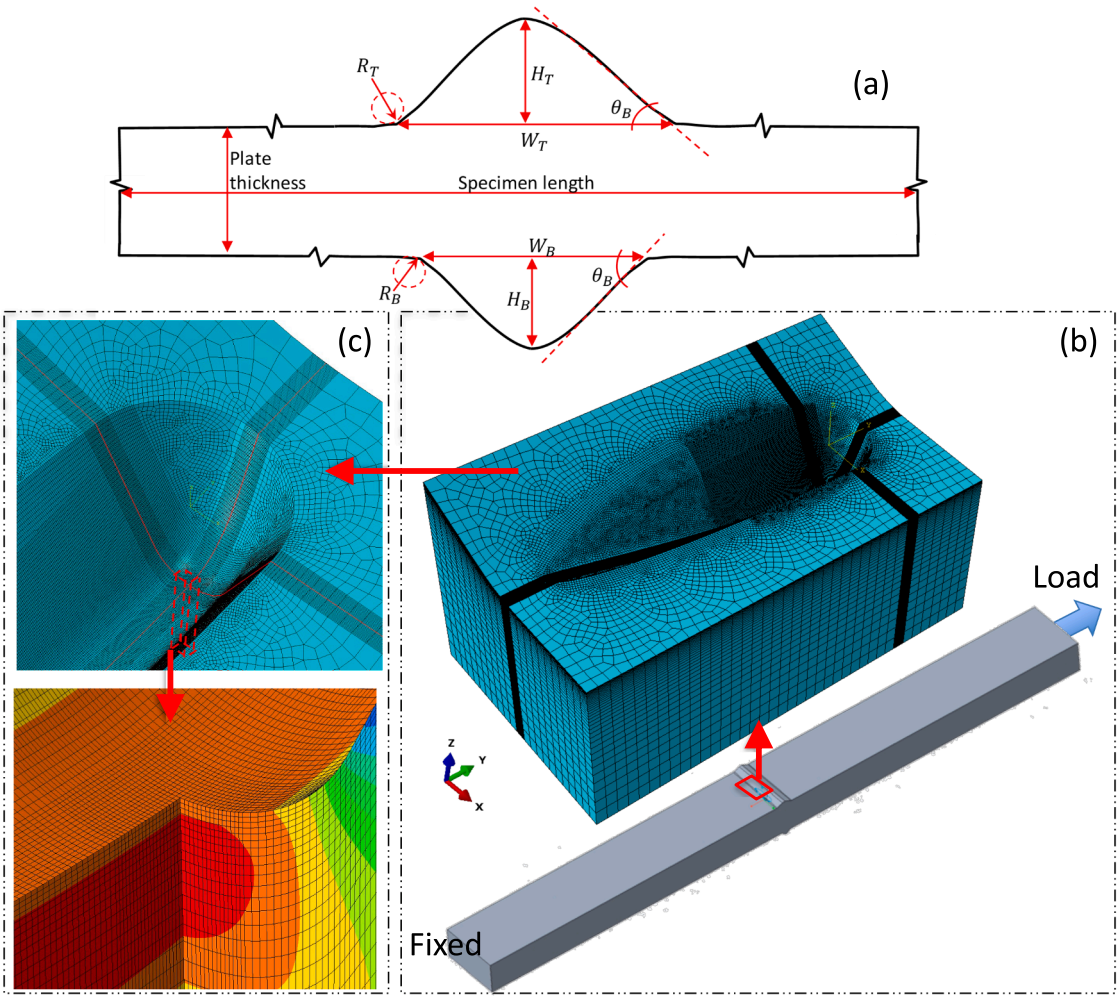

Fig. 6. (a) Global weld geometry, (b) Global weld model, undercut location, and local undercut sub-model, (c) Mesh at the undercut depth and along the thickness. The mesh is generated with a progressive increase in size away from the bottom of the undercut.

Table 2
Global weld geometry (see Fig. 6a).

Global geometry	Dimension	Global geometry	Dimension
Top weld height (H_T)	0.62 mm	Bottom weld height (H_B)	0.74 mm
Top weld width (W_T)	3.9 mm	Bottom weld width (W_B)	3 mm
Top weld toe radius (R_T)	0.66 mm	Bottom weld toe radius (R_B)	0.54 mm
Top weld flank angle (θ_T)	21.84 deg	Bottom weld flank angle (θ_B)	33 deg

4. Results

The systematic FEA of the undercut models with varied geometry is carried out to study the relation between the undercut geometry and fatigue performance. The current study performed cyclic 3D elasto-plastic FEA on 159 undercut models with different shapes and sizes. The validation of the modeling approach and the general stress–strain behavior of the undercut is presented in the sub-section below, followed by the influence of undercut asymmetry and undercut geometry parameters on fatigue crack initiation life. Finally, a 3D undercut geometry index is proposed.

4.1. Stresses and strains in local undercuts

The modeled undercut geometry was validated against a high-resolution scanned undercut geometry utilizing cyclic elasto-plastic FEA. A maximum difference of 3 % in averaged maximum principal stresses and 10 % in averaged maximum principal strains was observed, as shown in Fig. 10. The higher difference in strains compared to stress results from the plastic behavior predominating in the plastic zone of the undercut.

Fig. 11c shows the maximum principal stress and strain amplitude through the thickness of the undercut at the maximum depth location and the maximum principal stress location at the load level of 172 MPa. The maximum principal stresses were under the surface of the undercut (see the grey contour in Fig. 11b), and their location was not necessarily at the maximum undercut depth. The area of maximum principal stresses was frequently found towards the center of the undercut, as shown in Fig. 11b. Similarly, the strain amplitude (Fig. 11c) and SWT

Table 3
Isotropic and Kinematic hardening parameters for the Voce-Chaboche material model.

Material	E [GPa]	$\sigma_{y,0}$ [MPa]	Q_∞ [MPa]	b	C_1 [MPa]	γ_1	C_2 [MPa]	γ_2
S355J2	198.39	251.74	118.43	10.85	17876.51	236.3	2582.61	24.01

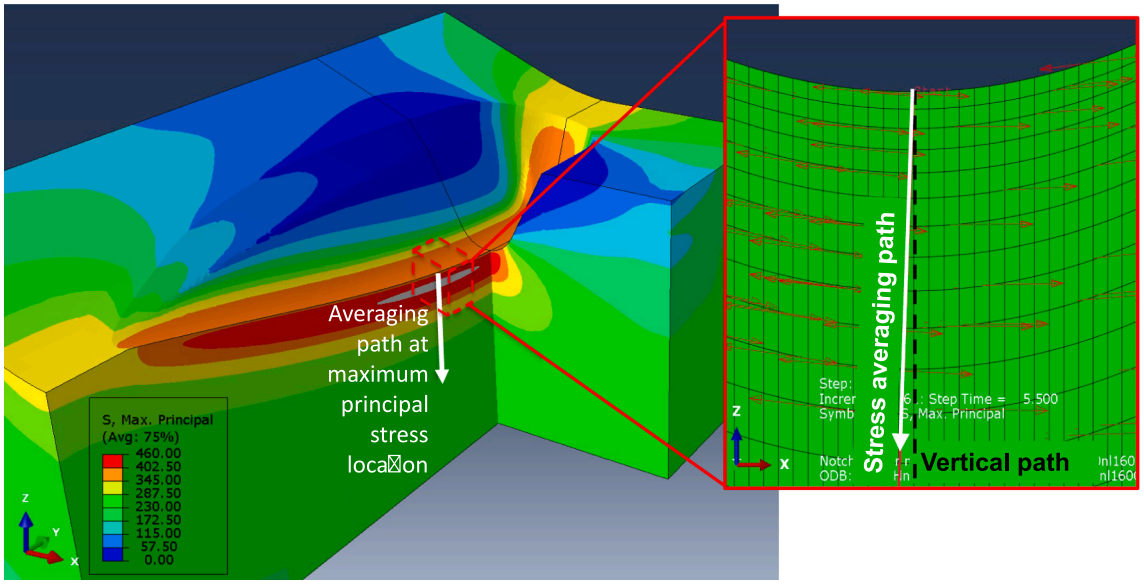

Fig. 7. 3D stress contour of undercut, stress averaging path, and mesh at the averaging volume unit location.

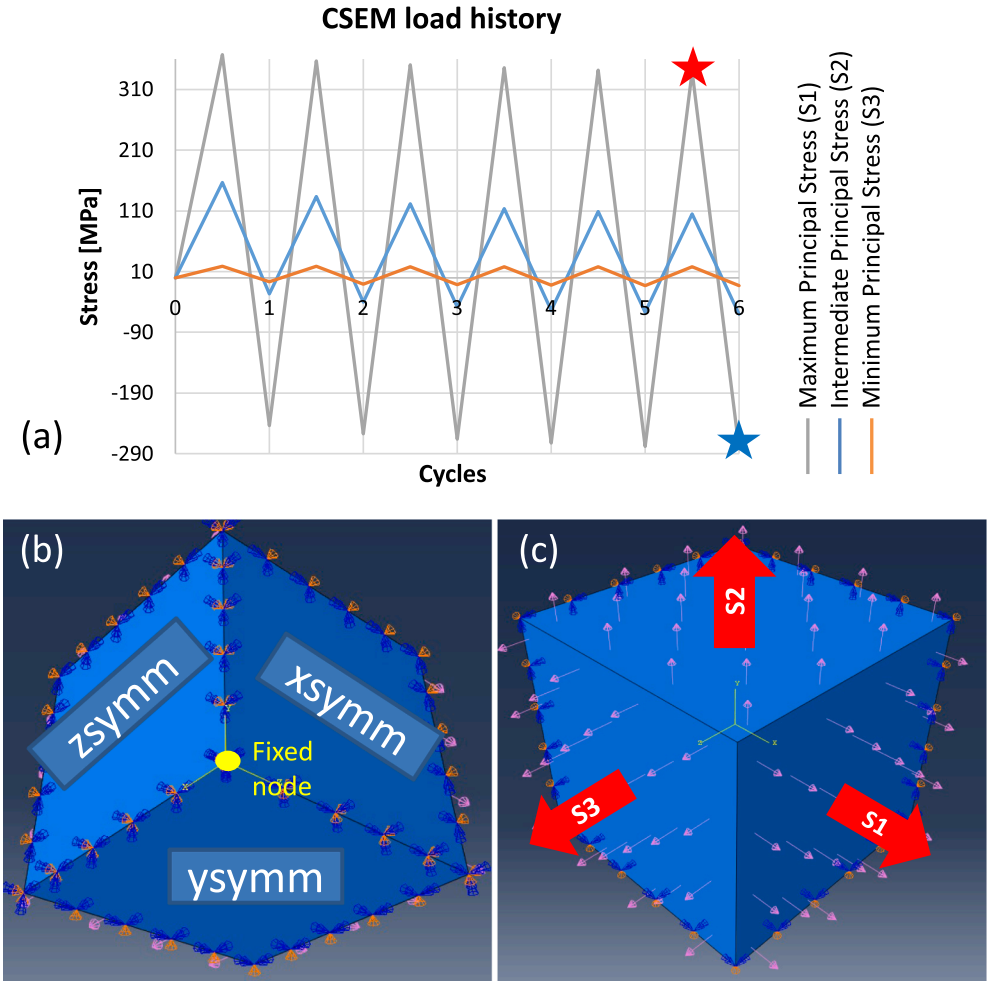

Fig. 8. Continuum single element model (CSEM) for strain range calculation. (a) Load history extracted from undercut sub-model, (b) boundary conditions for the CSEM model, and (c) load applied on CSEM.

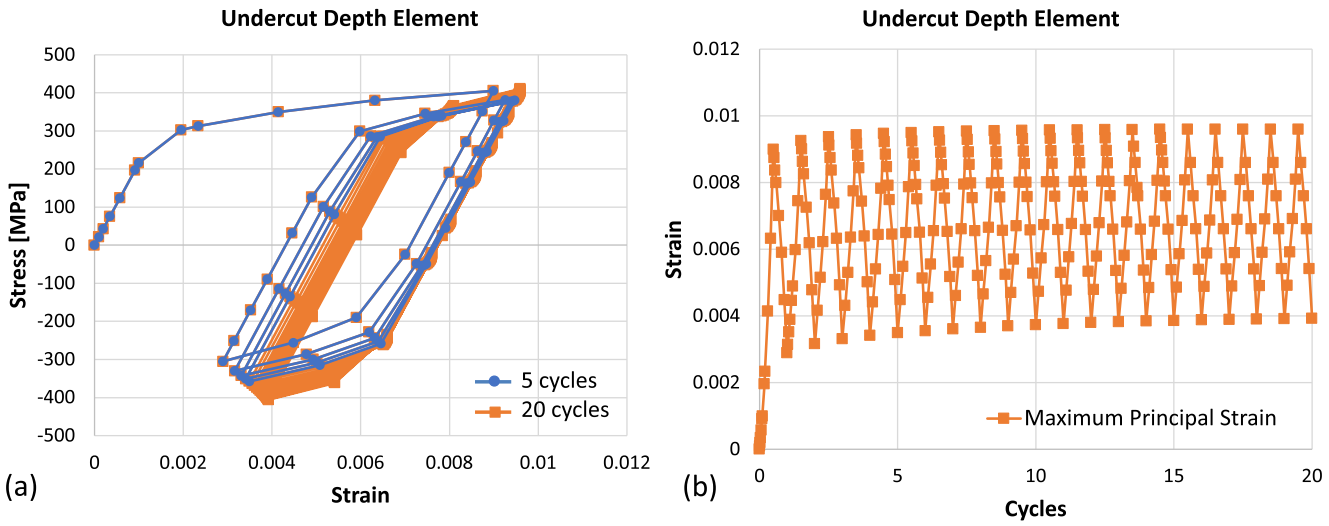

Fig. 9. (a) Stress-Strain curve from 5- and 20-cycle simulation of undercut model with the VC material model, and (b) maximum principal strain vs. cycles of the undercut depth element.

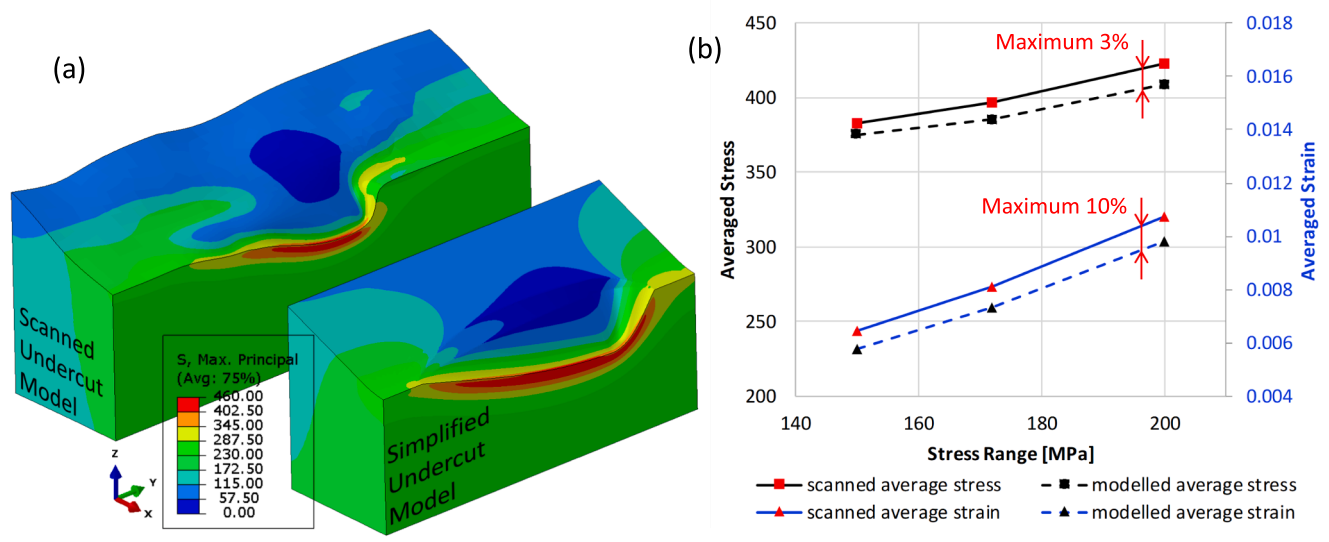

Fig. 10. (a) 3D FEA of scanned and simplified undercut geometry, and (b) averaged maximum principal stresses and strains at different applied stress ranges.

parameter (Fig. 11d) were highest at the undercut surface and frequently near the center of the undercut length. Therefore, the fatigue crack initiation life is estimated at the location of the maximum principal stress for each undercut model in the current investigation.

4.2. *Influence of undercut asymmetry*

The effect of undercut asymmetry on fatigue was systematically studied with undercut models of constant *d*, *r*, *w*, and *l* while varying the locations of the deepest point of the undercut. An example of the resulting undercut length profile is shown in Fig. 12c, and the respective 3D model in Fig. 13a. The asymmetry of the undercut influences the local notch constraint and plasticity, and thus, the stress and strain distribution. Fig. 12c shows an example of the undercut length profiles with total asymmetry of 0, 0.35, and 0.53, as well as the stresses and SWT parameter along the length of the undercut. An increase in the asymmetry leads to higher stresses and SWT, as shown in Fig. 12a-b, resulting in a reduced fatigue crack initiation life of asymmetric undercuts compared to the symmetric cases, as shown in Fig. 13b. Furthermore, the influence of asymmetry is more pronounced in deeper undercut, as shown in Fig. 13b. However, the variation in the SWT parameter is relatively small, i.e., 5 %.

4.3. *Influence of undercut geometry parameters*

The influence of each individual undercut geometry parameter, and several combinations of these parameters on fatigue crack initiation life was examined. ANOVA analysis was performed with Matlab R2023b software to check the statistical significance of the resulting relations ($p < 0.05$), and multiple regression analyses were performed to find the best relationship between the geometric definition of undercut and the fatigue crack initiation life.

Fig. 14a-e shows the plot of fatigue crack initiation life against the undercut's depth, radius, width, length, and opening angle. As shown in Fig. 14, despite the statistical significance, each individual geometric parameter cannot define the 3D undercut geometry and, therefore, does not correlate well with the fatigue crack initiation life of the undercut. However, they provide essential insight into the fatigue crack initiation life trend in the presence of the local undercut defects. The depth and length of the undercut display an inverse relationship to fatigue life as

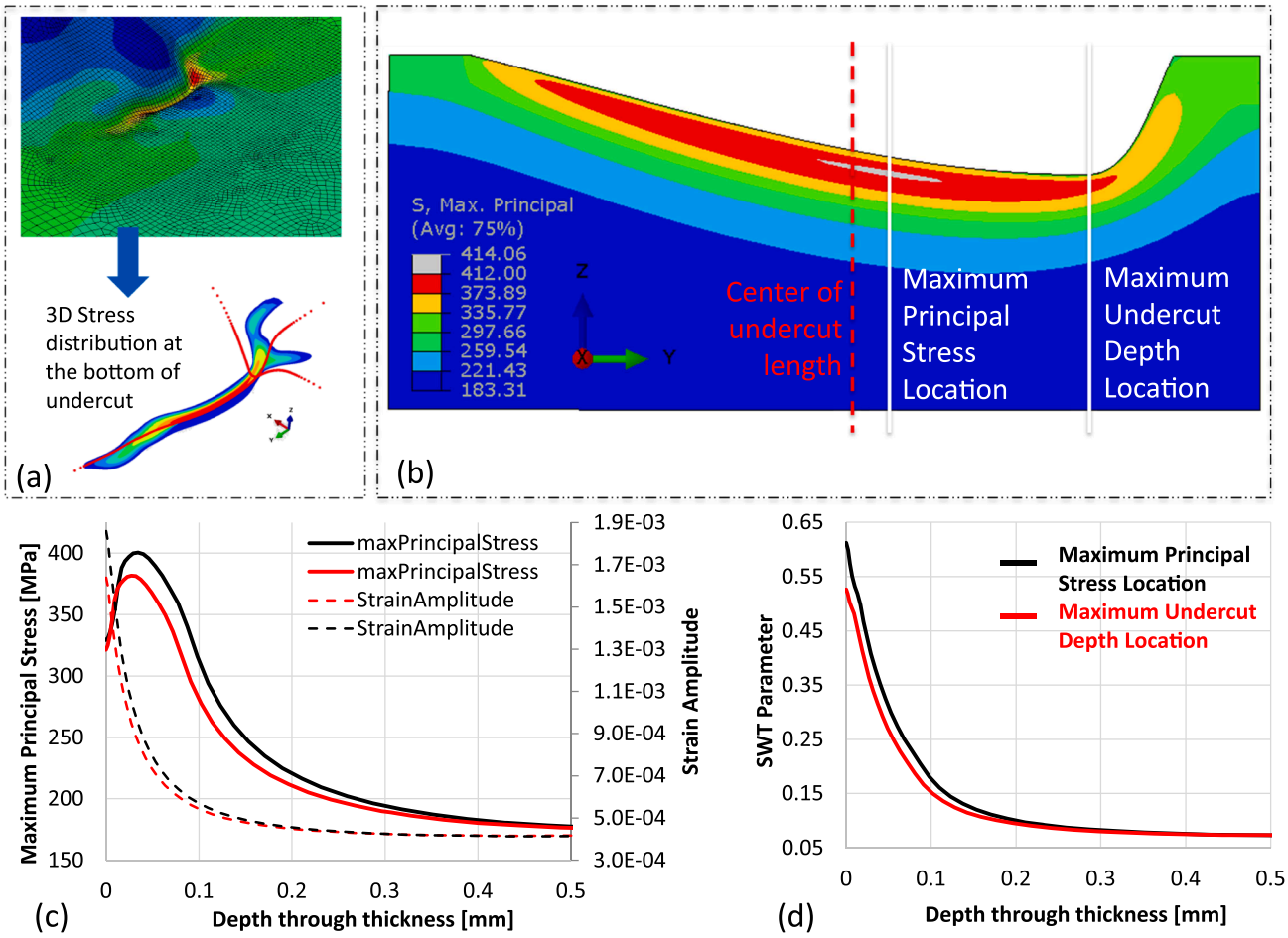

Fig. 11. (a) 3D stresses of undercut, (b) Maximum principal stress contour along the undercut length, (c-d) Maximum principal stress, strain amplitude, and SWT parameter through the thickness of the undercut at the maximum undercut depth location and the maximum principal stress location.

the increase in these parameters reduces the fatigue crack initiation life, while the undercut's radius, width, and opening angle show a direct relationship with fatigue crack initiation life. This influence is employed to combine the individual undercut geometry parameters to develop an equation that describes the 3D undercut geometry and shows a solid link to fatigue crack initiation life.

4.4. 3D undercut geometry indicator

As the individual geometry parameters are insufficient to describe the 3D undercut geometry, they were arithmetically combined to formulate new geometric indicators that can define the 3D undercut geometry and correlate with the fatigue crack initiation life. The statistical significance of the newly formulated geometric indicator was examined based on the ANOVA test, and the best-fitting indicator was determined as the 3D undercut geometry indicator. Some of the statistically significant geometric indices investigated in current study are presented in Appendix B. An example of an indicator is the ratio of the undercut depth to the undercut radius (d/r), which is widely used in the literature. Fig. 15 shows that the d/r parameter has a strong influence on the fatigue crack initiation life. However, the definition with d and r alone can only partially describe the 2D profile of an undercut, which is not sufficient to explain the 3D geometry.

At least four undercut geometry parameters are required to define the symmetric undercut geometry: d, r, w, and l. However, two more geometry parameters are needed to identify the location of the deepest point of undercut and fully define the 3D geometry of asymmetric undercuts: w_L and l_L. Equation 5 shows the relation of fatigue crack initiation life N_i and the 3D undercut geometry indicator ($\mathfrak{G}_{3D}$) defined with four parameters, corresponding to Fig. 16a and 16c. This representation can model symmetric undercuts but cannot distinguish between the asymmetric undercuts with similar four geometric parameters. On the other hand, equation 6 contains the geometric information of the asymmetry with the additional two parameters and corresponds to Fig. 16b and 16d. This representation can fully describe the symmetric as well as asymmetric undercut. In the current numerical investigation, the range of the ratio of undercut depth to undercut length varied from 2.1 to 27.5. However, in the following equations, undercut length is limited to a maximum of 10*d based on Liinalampi's work, where the undercuts with $l > 10$*d are reported to behave as a continuous undercut [30].

$$\log(N_i) = -0.865*\log\left(\left(\frac{d}{r}\right)^2 \frac{l}{w}\right) + 7.337, \text{ where } l \leq 10 * \text{d} \quad (5).$$

$$\log(N_i) = -0.863*\log\left(\left(\frac{d}{r}\right)^2 \frac{l}{w} * \sqrt{1 - asym}\right) + 7.273, \text{ where } l \leq 10 * \text{d} \quad (6).$$

4.5. 3D undercut index

The influence of the stress level on the fatigue crack initiation life was investigated with selected structural stress ranges (150 MPa, 172 MPa, and 200 MPa) and undercut geometry models to minimize the computational expenses. As expected, the results clearly indicate the influence of stress range on the fatigue crack initiation life of the undercuts. The fatigue crack initiation life reduces with increasing stress

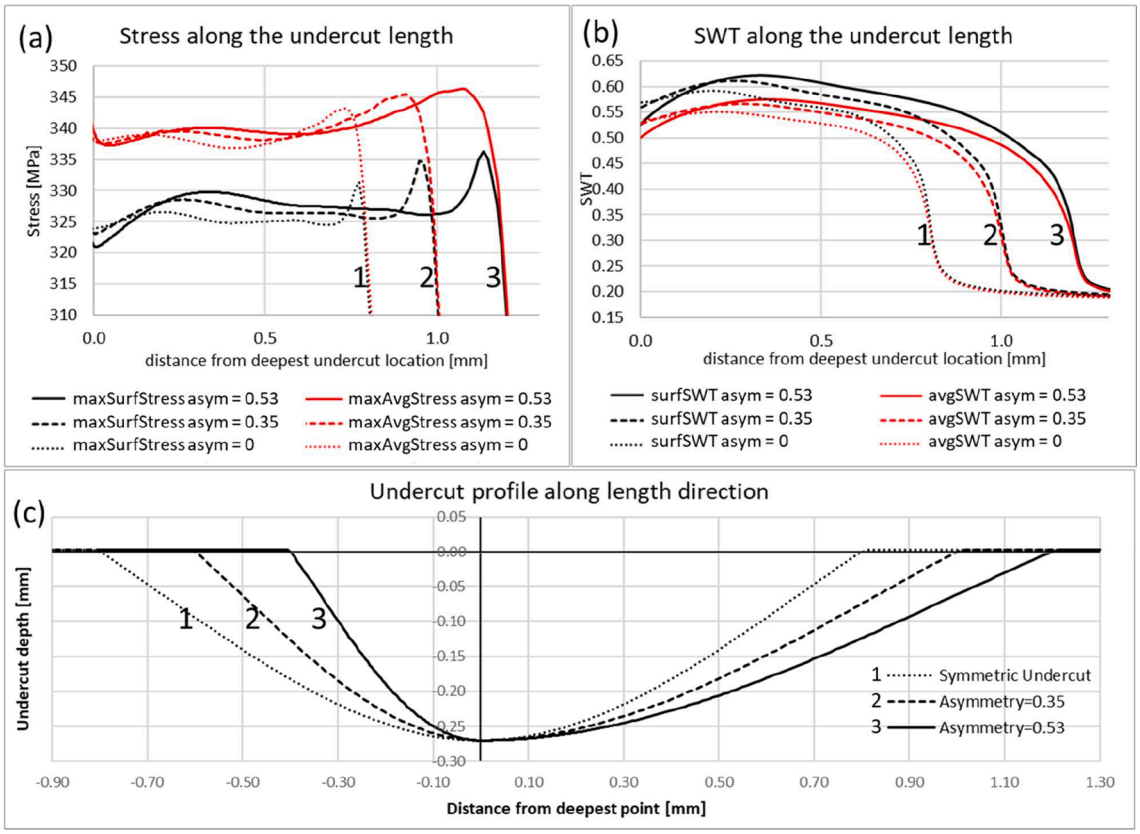

Fig. 12. (a-b) Comparison of stresses and SWT along the length of asymmetric and symmetric (asym = 0) undercuts, and (c) the geometric profiles of the undercut length.

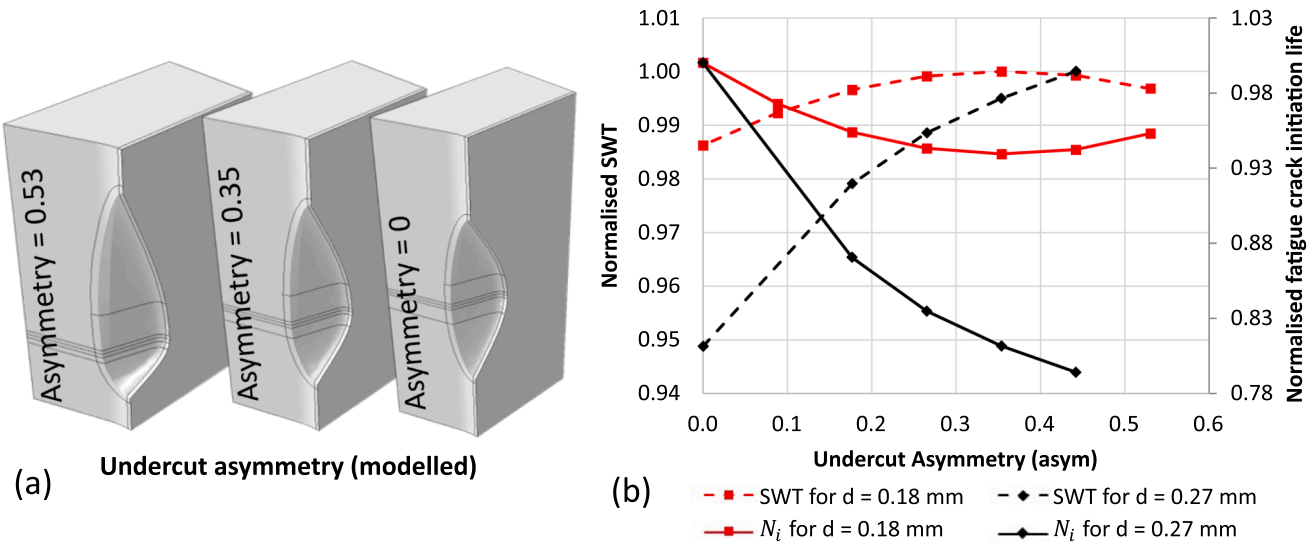

Fig. 13. Influence of undercut asymmetry on fatigue. (a) Examples of undercut models for asymmetry study, all the models have the same geometry parameters except the location of the deepest point, (b) influence of asymmetry at different undercut depths on SWT and fatigue crack initiation life.

range while following a consistent logarithmic relationship with an offset, as shown in Fig. 17a. To formulate the 3D undercut index (Ψ_{3D}) for general application (see equation (7), the 3D undercut geometry indicator is normalized by its maximum value, and the ratio of the applied structural stress range ($\Delta\sigma$) to the corresponding fatigue strength at 2 million load cycle, i.e., FAT 100 in the case of structural stress of butt welded joint of the current study. The maximum value of the 3D undercut geometry indicator ($\mho_{3D,max}$) is calculated within each series of investigation. An exponent of $m = 7$ is used to the $\Delta\sigma$/ FAT ratio to make the normalization suitable for fatigue crack initiation life. As shown in Fig. 17b, the 3D undercut index results in a single curve for the relationship between N_i and the index for all of the undercut models. Equation (8) shows the relation of the 3D undercut index to N_i from all undercut models corresponding to Fig. 17b.

$$\Psi_{3D} = \frac{\mho_{3D}}{\mho_{3D,max}} \left(\frac{\Delta\sigma}{FAT}\right)^{m} \tag{7}$$

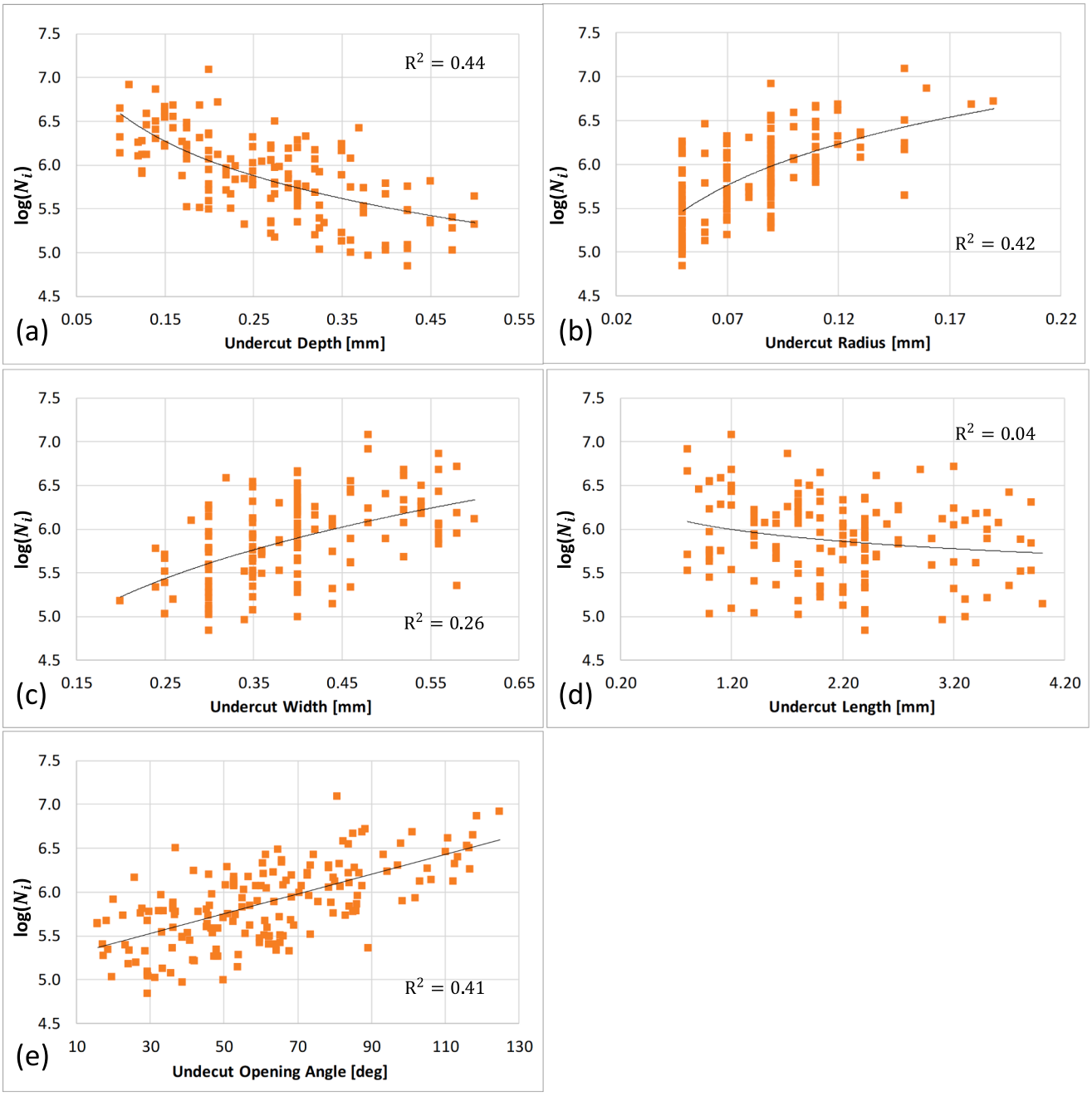

Fig. 14. (a-e) Fatigue crack initiation life vs. individual undercut geometry parameters.

where, $\mho_{3D} = \left(\frac{d}{r}\right)^2 \frac{l}{w}$ and m = 7 in current study.

$$\log(N_i) = -0.838*\log(\Psi_{3D}) + 6.389 \quad (8)$$

The proposed 3D undercut index is compared with fatigue test data from [3] and is plotted in Fig. 17b. The fatigue crack initiation life (N_i) of the fatigue tests is estimated utilizing their total fatigue life (N_f) from [3]. This estimation is based on the best-fitted relationship between N_i and N_f, derived from fatigue tests on similar laser-MAG hybrid butt joints presented in [37], where $N_i = 0.0007*N_f^{1.4956}$. This relationship considers the fact that the fatigue crack initiation time is shorter within the low cycle fatigue regime than that of the endurance limit ($N_f > 2*10^6$ cycles), where N_i is closer to N_f. The deviation of some fatigue test datapoints in Fig. 17b might have been a result of the interaction between multiple undercuts, or from possible material defects other than undercuts.

5. Discussion

A direct experimental investigation of local undercut geometry is not feasible, as preparing welded samples with specified undercut dimensions is impossible, primarily since they are known to have a stochastic appearance along the weld toe. Furthermore, the experimental investigation would have limited coverage in the study of possible geometric combinations of undercut with the limited undercuts present in the test welds. Therefore, the present study investigated the influence of the 3D geometry of local undercuts on the fatigue crack initiation life of a butt-welded steel joint by utilizing systematically designed undercut geometries and elasto-plastic cyclic FEA. The undercut imperfections

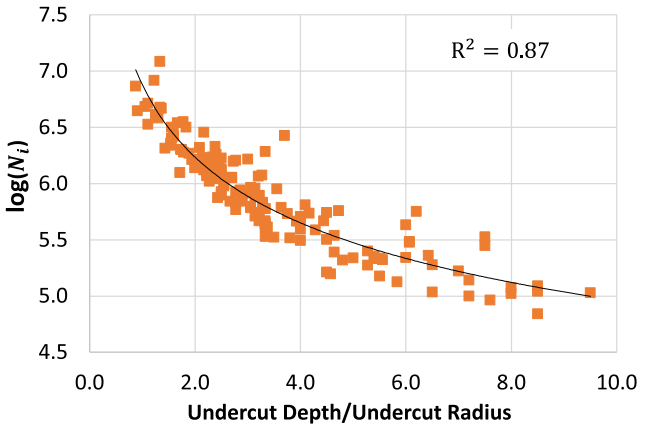

Fig. 15. The ratio of undercut depth and undercut radius vs. fatigue crack initiation life.

under investigation are within the depth of 0.5 mm and are within the allowable limit of undercut according to current standards [5,7,9], while they have been found detrimental to the fatigue life of high-performing welds in a recent study [3]. The present study results clarify the influence of the local undercut geometry on fatigue crack initiation life, and the main findings regarding the characterization and influence of the undercut geometry are presented and discussed below.

5.1. Characterization of the local undercut geometry

The existing literature and standards mostly recognize the depth and radius of the undercut [4–7]. In contrast, the width and length of the undercut are scarcely studied [30], resulting in a 1D or 2D definition of local undercut geometry despite the significant 3D presence. The 3D undercut geometry indicator defined in the current paper combines individual geometric parameters into one indicator. A robust definition of the 3D undercut geometry indicator ($\mho_{3D,asym}$) requires six geometry parameters (see Fig. 3c) and can define asymmetric and symmetric undercuts, as shown in equations (9) and (10). The asymmetry parameter (*asym*) is a normalized asymmetry value that ranges between zero for symmetric undercuts when $l_L = l/2$ and $w_L = w/2$, and one for highly asymmetric undercuts. The asymmetry value of one is physically impossible in an undercut as the deepest point of the undercut cannot be perfectly under the edge of the undercut opening. On the other hand, the simplified symmetric 3D undercut geometry indicator definition is a particular case when $asym = 0$ and suffices with four parameters, as shown in equation (11).

Asymmetric 3D undercut geometry indicator $(\mho_{3D,asym})$

$$= \left(\left(\frac{d}{r} \right)^2 \cdot \left(\frac{l}{w} \right) \right) * \sqrt{1 - asym} \tag{9}$$

Where

$$asym = \sqrt{\frac{1}{2}\left[\left(1 - \frac{2l_L}{l} \right)^2 + \left(1 - \frac{2w_L}{w} \right)^2 \right]} \tag{10}$$

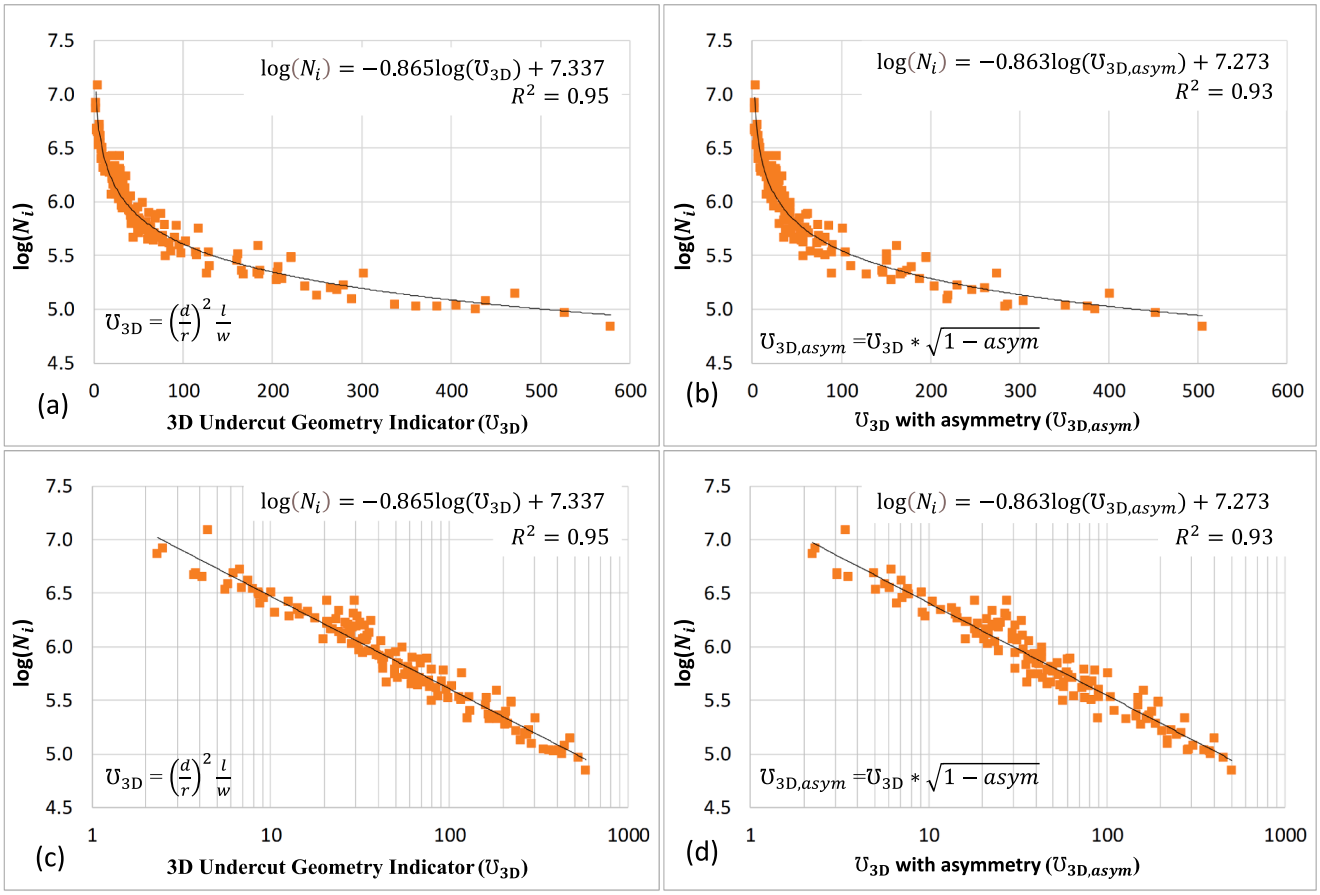

Fig. 16. 3D undercut geometry indicator vs. fatigue crack initiation life: (a) and (c) show the indicator with four parameters that represent symmetric undercuts, and (b) and (d) with six parameters that can model asymmetric undercut models.

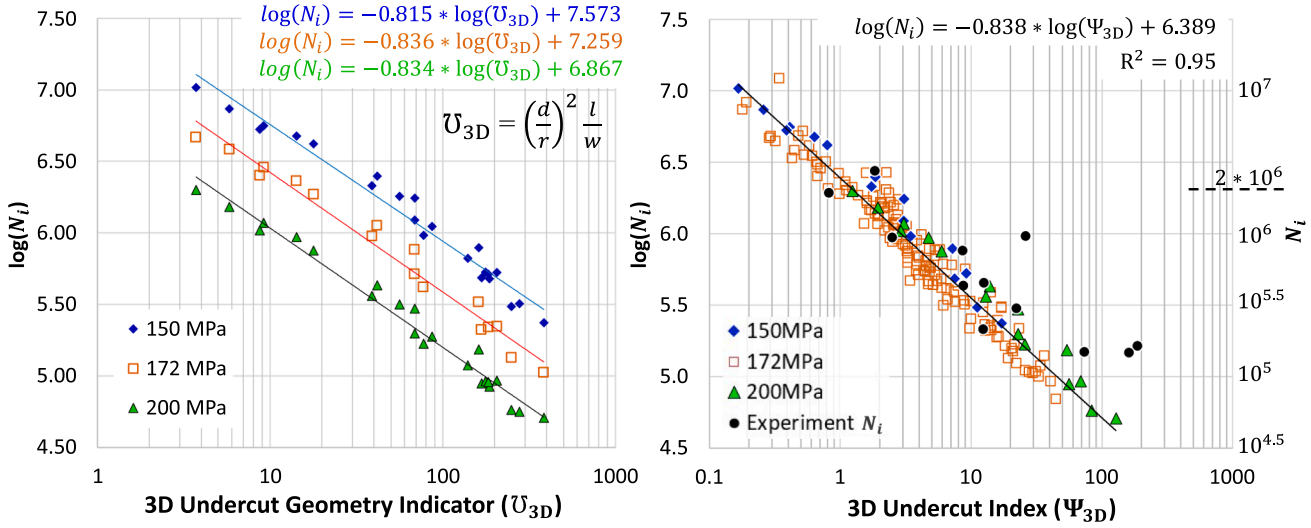

Fig. 17. (a) Fatigue crack initiation life at three stress ranges: 150 MPa, 172 MPa, and 200 MPa, (b) 3D undercut index vs. fatigue crack initiation life for different stress ranges with experimental data.

$$\textit{Symmetric 3D undercut geometry indicator } (\mho_{3D}) = \left(\left(\frac{d}{r}\right)^2 \cdot \left(\frac{l}{w}\right)\right) \tag{11}$$

The increase in the undercut opening angle reduces the geometric gradient at the bottom of the undercut and vice-versa, indicating the sharpness of an undercut. The undercut radius (r), and the ratio of undercut depth to undercut radius (d/r) have a theoretical significance in describing the sharpness of the notch [38]. However, the radius measurement in practice has its challenges, as pointed out by several researchers [2,3,13,14]. Meanwhile, the measurements of d and w are more robust and well-established as they are linear length measures on a straight path. The ratio of undercut depth to undercut width (d/w) shows a significantly stronger relation to the undercut opening angle, as shown in Fig. 5c-d, in comparison to the d/r ratio. This suggests that the undercut sharpness definition with the ratio of d/w introduced in the current study is more robust in practical industrial applications.

5.2. Influence of undercut geometry on fatigue performance

Among the individual geometry parameters, the undercut depth has a deteriorating effect on fatigue. In contrast, an increase in the undercut radius increases fatigue life, as shown in Fig. 14a-b. These observations are consistent with the literature [3,25,28,39–42]. Among the geometric control parameters of the current study, the undercut depth was found to be the best indicator for fatigue performance using numerical simulations, agreeing with the previously published experimental results [3]. The current study found that the undercut radius and undercut opening angle were the next best indicators for describing the fatigue performance. Furthermore, the undercut opening angle measured from the undercut models positively correlated to the fatigue crack initiation life. The increase in the undercut opening angle reduces the geometric gradient at the bottom of the undercut, making it blunter. This correlates to an increase in fatigue crack initiation life, as shown in Fig. 14e. This agrees with the literature where the increase in undercut opening angle has been reported to reduce stresses [37,43], which results in higher fatigue life. Increasing undercut width shows improvement in fatigue life while the undercut length deteriorates it, but neither parameter strongly correlates to the fatigue crack initiation life, as shown in Fig. 14c-d. However, despite explaining the influence on the fatigue crack initiation life, individual geometric parameters cannot distinguish between various undercuts or adequately describe the 2D or 3D undercut geometry.

The current paper demonstrates a significant improvement in fatigue crack initiation life prediction with additional undercut geometry parameters. The ratio of undercut depth and undercut radius (d/r) is commonly used in the literature [10–12] and demonstrated a good correlation to the fatigue crack initiation life in the current study, as shown in Fig. 15. It is a suitable parameter to partially describe the shape of 2D and continuous undercut, but the two parameters are not enough to represent the local 3D undercut geometry. The undercut geometry indicator, as a function of the four undercut geometry parameters, i.e., depth, radius, length, and width of undercut, was found to successfully represent the 3D undercut geometry for symmetric undercuts. The undercut opening angle is excluded in the formulation of the 3D undercut geometry indicator as it results from the undercut shape formed by the four undercut geometry parameters and is already indirectly included in the formulation. The undercut geometry indicator, defined with four geometry parameters, correlates well with the fatigue crack initiation life, as shown in equation 5, with the R^2 value of 0.95; see Fig. 16a.

On further investigation, adding an asymmetry parameter to the undercut geometry indicator enhanced its robustness in defining and differentiating the asymmetric undercuts with matching depth, radius, length, and width parameters. Such a comprehensive relation of the undercut geometric parameters to fatigue crack initiation life can be utilized in fatigue-based weld quality control. However, the superior robustness of the undercut geometry definition requires two additional geometry parameters for the definition of the asymmetry indicator (see Fig. 2 and Fig. 3c), which results in a slight increase in the scatter in the current study. Equation 6 shows the relation of undercut geometry parameters along with the asymmetry indicator to the fatigue crack initiation life with the R^2 value of 0.93, as shown in Fig. 16b.

Despite the minor influence of undercut asymmetry on the fatigue crack initiation life, modeling an asymmetric undercut is more laborious, requires two additional geometric parameters, and the simulations are computationally demanding compared to the symmetric undercut. Furthermore, the influence of asymmetry on fatigue is not highly significant when other geometry parameters, such as undercut depth, radius, width, and length, are considered. Therefore, utilization of the symmetric 3D undercut parameter, as shown in Equation (11), and the corresponding relation to fatigue crack initiation, as shown in Equation 5, is justified in industrial applications for the fatigue assessment of undercut defects.

The 3D undercut index proposed in equation (7) includes the 3D

undercut geometry with d, r, w, l, and the applied structural stress range for the undercut. An exponent of $m = 7$ for the 3D undercut index led to the best fit for the fatigue crack initiation life with the different structural stress ranges in the current study. This is in line with the experimental observation in literature where the slope of the SN curve for fatigue crack initiation is shallower compared to the total fatigue life [37,44]. The 3D undercut index shows a strong relation with the fatigue crack initiation life, and it unifies the influence of structural stress range into a single curve represented by the equation (8) with an R^2 of 0.95, as shown in Fig. 17b. The result is compared to the fatigue crack initiation life from fatigue tests of [3] in Fig. 17b, and it shows an excellent agreement at high cycles towards the endurance limit and a conservative result at the lower cycles. It can provide a comparative estimation for the fatigue crack initiation life of an arbitrary undercut geometry for a given structural stress range and assist in the fatigue-based fitness-for-purpose assessment of welded structures.

6. Conclusion

The present study focused on simplified modeling of the three-dimensional undercut geometry based on experimentally measured high-resolution and high-accuracy geometry data from laser-MAG hybrid butt welds. Cyclic elasto-plastic nonlinear FEA was performed utilizing the built-in Voce-Chaboche material model of Abaqus solver with the undercut geometry models, and the correlations of the undercut geometry to fatigue crack initiation life were investigated.

In the geometry measurements, plenty of undercuts were found to be asymmetric and would require scanned data or a large number of geometric parameters to model the undercut geometry. The current study showed that the 3D undercut shape can be simplified with four geometric parameters (d, r, l and w) for symmetric undercuts, and an additional two parameters (w_L and l_L) are required for asymmetric undercuts. The three-dimensional description of the undercut significantly improved the fatigue crack initiation life estimation than individual geometric parameter like d, or incomplete 2D geometric descriptions like d/r. The 3D description of undercut geometry also enables quality-based characterization of different undercuts as it can differentiate between various undercut geometries. The asymmetry of the undercut reduced the fatigue crack initiation life, and the influence of asymmetry was more pronounced in the deeper undercut. However, the influence of asymmetry was small in comparison to other geometric parameters (such as d, r, l and w) and required additional geometry parameters for analyses. Therefore, undercut geometry can be simplified with four geometric parameters for industrial applications and quality purposes.

Undercuts have a larger radius in comparison to a crack, and the undercut opening angle provides a good indication of undercut sharpness. The current study demonstrated that deeper undercuts have a sharper undercut opening angle. Furthermore, the undercut opening angle has a much stronger relation to the d/w parameter (R^2 value of 0.94) in realistic undercuts compared to the traditionally used d/r parameter (R^2 value of 0.53). The measurement of d/w is also more robust and applicable in engineering practice than the d/r parameter and the undercut opening angle. Therefore, it is a more suitable geometric parameter to describe the undercut sharpness for industrial application and quality control purposes.

Modern automated weld facilities can produce consistently high-quality welds; however, the stochastic presence of shallow and blunt undercut defects is not allowed in standards and demands a large amount of repair work despite their low detrimental effect on fatigue life. A detailed description of undercut quality based on the 3D undercut index could reduce the costly repair works and promote more environmentally friendly production of welded components. The undercut defects designed for the current study were based on experimental observations on butt welds. Thus, investigating different joint types, plate thickness, and the transition undercut length where the local undercut behaves as a continuous undercut is recommended for future work.

CRediT authorship contribution statement

Abinab Niraula: Writing – review & editing, Writing – original draft, Visualization, Validation, Methodology, Investigation, Funding acquisition, Formal analysis, Conceptualization. **Heikki Remes:** Writing – review & editing, Supervision, Resources, Funding acquisition, Conceptualization. **Alain Nussbaumer:** Writing – review & editing, Supervision, Resources.

Declaration of competing interest

The authors declare that they have no known competing financial interests or personal relationships that could have appeared to influence the work reported in this paper.

Data availability

Data will be made available on request.

Acknowledgements

This research was funded by Aalto University, Meyer Turku Oy, and the CaNeLis project (funding from Business Finland under grant No. 3409/31/2022). The financial support is gratefully acknowledged. Sincere thanks to RESSLab in École Polytechnique Fédérale de Lausanne (EPFL) for providing resources and support during the research visit, the Solid Mechanics Laboratory of Aalto University and Pauli Lehto for valuable comments and support in the fatigue experiments, and CSC – IT Center for Science for providing ABAQUS license and computational resources for the simulations.

Appendix

Appendix A

The six undercut geometry parameters needed to create the undercut geometry are presented in Table A1 below. Table A2 shows the results from selected undercut models investigated with three different structural stress ranges. In addition to the geometry data, each table contains the averaged maximum principal stress (σ_{max}) and strain amplitude (ε_a) for the each undercut model along with the resulting fatigue crack initiation life N_i. In current investigation, the R-ratio is kept 0 for all the cases.

Table A1
Geometry parameters for the local undercut models of current investigation, and the resulting fatigue crack initiation life with a 172 MPa stress range.

sn	d [mm]	r [mm]	w_L [mm]	w [mm]	l_L [mm]	l [mm]	σ_{max} [MPa]	ε_a	N_i
1	0.100	0.110	0.175	0.400	0.650	2.000	340.2194	1.273E-03	4,431,402
2	0.100	0.050	0.150	0.300	0.650	1.800	356.6241	1.566E-03	1,378,322
3	0.100	0.070	0.150	0.350	0.650	1.800	348.5648	1.464E-03	2,065,402
4	0.100	0.090	0.150	0.400	0.850	1.800	343.8401	1.335E-03	3,363,322
5	0.110	0.090	0.200	0.480	0.350	0.800	359.6822	1.060E-03	8,260,202
6	0.120	0.070	0.150	0.280	1.650	3.300	358.8941	1.590E-03	1,256,082
7	0.120	0.050	0.225	0.420	0.650	1.700	355.8527	1.476E-03	1,811,702
8	0.125	0.050	0.125	0.350	0.850	2.400	344.7945	1.845E-03	790,062
9	0.125	0.050	0.150	0.350	1.050	2.200	338.0884	1.853E-03	843,242
10	0.125	0.050	0.175	0.350	0.450	1.400	357.2338	1.578E-03	1,324,782
11	0.125	0.070	0.125	0.300	0.250	1.200	346.3617	1.501E-03	1,896,382
12	0.130	0.060	0.175	0.440	0.700	2.400	341.0505	1.654E-03	1,320,782
13	0.130	0.060	0.150	0.460	0.250	0.900	338.6857	1.404E-03	2,856,382
14	0.130	0.100	0.150	0.320	0.550	1.100	338.2703	1.320E-03	3,827,682
15	0.140	0.080	0.175	0.380	0.900	1.800	375.1768	1.369E-03	2,001,262
16	0.140	0.090	0.200	0.500	0.400	1.800	344.1291	1.420E-03	2,517,022
17	0.140	0.090	0.200	0.540	0.800	1.900	345.4832	1.346E-03	3,162,962
18	0.140	0.160	0.275	0.560	0.750	1.700	347.4781	1.123E-03	7,355,402
19	0.150	0.110	0.150	0.400	0.250	0.800	340.1576	1.260E-03	4,657,662
20	0.150	0.050	0.300	0.400	0.650	1.400	335.6388	1.598E-03	1,651,262
21	0.150	0.070	0.250	0.400	0.450	1.800	336.0790	1.586E-03	1,695,522
22	0.150	0.090	0.175	0.350	0.450	1.000	368.2246	1.238E-03	3,480,262
23	0.150	0.120	0.225	0.520	1.150	2.500	368.1633	1.194E-03	4,122,762
24	0.160	0.100	0.300	0.460	1.750	3.700	350.5042	1.378E-03	2,655,222
25	0.160	0.090	0.175	0.460	0.400	1.000	345.1787	1.315E-03	3,546,122
26	0.160	0.120	0.175	0.560	0.400	1.200	374.1283	1.139E-03	4,791,862
27	0.170	0.070	0.125	0.380	1.200	2.700	359.8346	1.791E-03	749,502
28	0.170	0.090	0.200	0.540	0.800	2.700	342.5421	1.526E-03	1,853,162
29	0.175	0.110	0.200	0.350	0.450	1.200	340.8502	1.376E-03	3,042,982
30	0.175	0.110	0.250	0.400	0.650	2.000	350.9754	1.378E-03	2,637,562
31	0.175	0.050	0.150	0.250	0.450	2.000	349.9340	2.262E-03	332,602
32	0.175	0.070	0.175	0.300	0.250	1.000	337.6926	1.580E-03	1,689,422
33	0.175	0.070	0.175	0.400	0.450	1.600	345.5054	1.681E-03	1,164,262
34	0.175	0.070	0.250	0.350	0.850	2.000	335.8339	1.672E-03	1,347,342
35	0.175	0.090	0.225	0.400	0.850	2.200	395.6879	1.358E-03	1,635,822
36	0.190	0.050	0.200	0.340	1.850	3.800	359.3406	2.211E-03	328,182
37	0.190	0.110	0.225	0.400	1.600	3.900	351.4089	1.459E-03	2,022,162
38	0.190	0.180	0.275	0.520	0.700	2.900	344.7143	1.234E-03	4,841,482
39	0.200	0.130	0.200	0.400	1.050	2.400	350.8583	1.420E-03	2,303,462
40	0.200	0.130	0.200	0.400	0.650	2.400	378.1116	1.332E-03	2,186,262
41	0.200	0.050	0.125	0.250	0.250	0.800	367.3523	1.928E-03	510,862
42	0.200	0.050	0.125	0.300	0.850	1.800	363.4422	2.086E-03	391,962
43	0.200	0.070	0.150	0.350	0.650	1.400	350.3344	1.773E-03	873,822
44	0.200	0.090	0.125	0.350	0.450	1.400	335.8554	1.725E-03	1,174,122
45	0.200	0.050	0.075	0.360	0.550	1.800	342.4597	2.349E-03	312,842
46	0.200	0.060	0.125	0.240	0.800	2.000	403.5861	1.686E-03	599,382
47	0.200	0.090	0.225	0.420	0.800	1.900	385.2415	1.432E-03	1,453,922
48	0.200	0.150	0.250	0.480	0.250	1.200	370.4226	9.520E-04	12,177,622
49	0.210	0.090	0.125	0.600	0.700	3.100	365.7463	1.543E-03	1,318,022
50	0.210	0.190	0.325	0.580	1.300	3.200	339.4134	1.235E-03	5,195,122
51	0.220	0.070	0.200	0.360	1.050	2.500	385.4741	1.836E-03	512,762
52	0.220	0.070	0.325	0.460	1.450	3.500	368.3514	1.736E-03	773,042
53	0.220	0.070	0.150	0.560	0.450	2.000	370.2151	1.661E-03	910,322
54	0.225	0.050	0.250	0.350	0.450	2.000	348.7928	2.293E-03	319,722
55	0.225	0.070	0.200	0.350	0.650	2.400	344.7532	2.104E-03	465,562
56	0.225	0.090	0.275	0.400	1.050	2.200	406.2282	1.429E-03	1,165,962
57	0.230	0.070	0.150	0.560	1.050	2.700	395.2399	1.670E-03	678,942
58	0.230	0.090	0.225	0.420	0.850	3.500	352.4599	1.714E-03	981,462
59	0.240	0.050	0.100	0.440	1.250	3.200	403.1572	2.227E-03	209,602
60	0.240	0.090	0.275	0.400	1.050	3.900	418.9627	1.565E-03	697,042
61	0.250	0.110	0.175	0.400	0.450	2.200	399.9816	1.488E-03	1,048,422
62	0.250	0.090	0.125	0.300	0.650	2.400	364.1856	1.877E-03	589,102
63	0.250	0.090	0.125	0.400	0.850	2.200	363.8320	1.817E-03	675,162
64	0.250	0.090	0.175	0.400	0.450	1.400	344.2004	1.567E-03	1,610,062
65	0.250	0.090	0.275	0.400	1.050	2.400	344.4402	1.817E-03	846,882
66	0.250	0.120	0.275	0.540	0.700	2.000	372.8450	1.364E-03	2,095,022
67	0.260	0.110	0.250	0.440	0.550	2.400	372.1163	1.580E-03	1,103,102
68	0.270	0.060	0.100	0.300	1.550	3.500	399.2537	2.413E-03	164,022
69	0.270	0.050	0.100	0.460	0.550	2.000	376.5505	2.365E-03	215,982
70	0.270	0.050	0.325	0.580	1.600	3.700	368.5281	2.385E-03	226,422
71	0.270	0.080	0.200	0.460	1.150	3.400	358.4663	2.088E-03	411,782
72	0.270	0.100	0.350	0.560	1.250	3.200	358.9708	1.630E-03	1,125,802
73	0.270	0.100	0.300	0.560	1.050	2.600	372.4466	1.567E-03	1,138,622
74	0.270	0.110	0.375	0.540	0.900	2.500	411.3094	1.324E-03	1,540,262
75	0.270	0.120	0.250	0.520	1.100	2.700	407.7517	1.314E-03	1,655,362

(*continued on next page*)

Table A1 (*continued*)

sn	d [mm]	r [mm]	w_L [mm]	w [mm]	l_L [mm]	l [mm]	σ_{max} [MPa]	ε_a	N_i
76	0.275	0.150	0.200	0.400	0.450	1.200	394.7619	1.177E-03	3,177,722
77	0.275	0.050	0.075	0.200	0.850	1.800	404.7847	2.441E-03	150,442
78	0.275	0.070	0.100	0.400	0.650	1.600	387.1252	1.877E-03	462,342
79	0.275	0.090	0.150	0.300	0.650	1.600	388.0454	1.747E-03	609,302
80	0.275	0.090	0.175	0.300	0.250	1.000	383.4112	1.597E-03	927,182
81	0.275	0.090	0.175	0.350	0.250	1.600	383.9513	1.754E-03	625,682
82	0.280	0.110	0.250	0.400	0.950	2.400	384.3221	1.585E-03	948,422
83	0.290	0.090	0.125	0.440	0.600	2.100	378.1255	1.838E-03	551,262
84	0.290	0.100	0.200	0.380	0.550	2.300	376.7209	1.741E-03	697,822
85	0.290	0.090	0.125	0.500	0.700	3.000	373.3020	1.709E-03	781,882
86	0.290	0.130	0.275	0.520	1.300	3.600	361.8789	1.596E-03	1,191,422
87	0.290	0.130	0.225	0.580	0.800	3.500	359.9142	1.515E-03	1,534,502
88	0.300	0.050	0.250	0.350	0.450	2.000	358.6125	2.468E-03	220,742
89	0.300	0.050	0.275	0.350	0.450	1.000	357.2616	2.071E-03	430,442
90	0.300	0.090	0.125	0.250	0.250	1.000	354.7072	2.043E-03	466,662
91	0.300	0.090	0.125	0.300	0.450	1.600	357.5930	1.904E-03	598,702
92	0.300	0.090	0.200	0.400	0.700	1.100	353.7139	1.464E-03	1,927,462
93	0.300	0.090	0.200	0.380	0.900	3.900	352.1278	2.236E-03	339,522
94	0.300	0.070	0.175	0.300	1.100	3.000	352.9127	2.154E-03	387,622
95	0.300	0.090	0.150	0.460	0.750	3.200	356.9262	2.090E-03	416,822
96	0.300	0.080	0.175	0.360	0.750	1.600	355.9886	1.962E-03	539,902
97	0.300	0.110	0.200	0.400	0.700	1.800	349.8591	1.548E-03	1,580,082
98	0.310	0.050	0.175	0.360	0.350	1.100	348.1801	1.984E-03	565,262
99	0.310	0.130	0.300	0.520	1.050	2.200	345.6783	1.464E-03	2,141,182
100	0.320	0.070	0.125	0.260	1.600	3.300	353.1158	2.763E-03	157,002
101	0.320	0.080	0.275	0.520	1.200	2.500	341.2456	2.109E-03	479,742
102	0.320	0.090	0.350	0.580	0.800	2.300	349.2353	1.768E-03	894,802
103	0.320	0.100	0.275	0.560	0.750	1.800	343.2944	1.693E-03	1,159,602
104	0.320	0.150	0.325	0.540	1.200	3.400	341.8349	1.604E-03	1,494,742
105	0.325	0.110	0.150	0.300	0.650	1.400	345.9924	1.821E-03	822,122
106	0.325	0.050	0.150	0.250	0.850	2.400	341.2137	3.197E-03	108,342
107	0.325	0.050	0.250	0.400	0.850	2.000	341.9713	2.700E-03	189,882
108	0.325	0.070	0.150	0.250	0.850	2.400	339.5087	2.528E-03	246,602
109	0.325	0.070	0.175	0.300	0.250	1.200	340.5172	2.300E-03	346,362
110	0.330	0.060	0.125	0.240	0.900	2.400	339.2361	2.624E-03	216,102
111	0.350	0.150	0.200	0.400	0.450	1.600	338.3130	1.629E-03	1,460,522
112	0.350	0.050	0.100	0.350	0.850	2.000	337.3713	2.841E-03	166,962
113	0.350	0.060	0.150	0.300	0.750	2.200	336.2396	3.042E-03	133,842
114	0.350	0.110	0.250	0.560	1.300	3.800	348.6627	1.841E-03	762,462
115	0.350	0.150	0.275	0.480	1.300	3.200	340.5297	1.559E-03	1,726,702
116	0.360	0.050	0.225	0.400	1.250	3.300	351.9828	3.180E-03	99,722
117	0.360	0.050	0.150	0.440	1.550	4.000	340.8241	2.966E-03	139,162
118	0.360	0.080	0.225	0.360	0.200	1.000	332.6072	2.089E-03	551,802
119	0.360	0.110	0.225	0.480	0.550	1.500	332.7211	1.736E-03	1,189,822
120	0.370	0.100	0.325	0.560	0.550	1.200	336.4730	1.434E-03	2,664,582
121	0.375	0.050	0.125	0.350	0.250	0.800	334.9221	2.356E-03	336,722
122	0.375	0.050	0.150	0.350	0.450	1.000	333.6283	2.481E-03	281,322
123	0.375	0.090	0.125	0.300	0.450	1.000	330.9890	2.107E-03	543,142
124	0.380	0.050	0.200	0.340	1.050	3.100	353.3162	3.244E-03	92,422
125	0.400	0.110	0.175	0.400	1.050	2.400	342.1138	1.979E-03	611,742
126	0.400	0.050	0.150	0.300	0.850	1.800	344.0530	3.197E-03	105,462
127	0.400	0.050	0.075	0.350	0.650	2.400	336.8363	3.148E-03	118,742
128	0.400	0.090	0.200	0.350	0.650	1.600	333.0093	2.176E-03	466,722
129	0.425	0.050	0.125	0.300	0.450	1.400	332.0459	3.266E-03	110,342
130	0.425	0.050	0.125	0.300	0.850	2.400	341.9806	3.675E-03	69,422
131	0.425	0.050	0.175	0.300	0.250	1.200	340.2327	3.081E-03	123,442
132	0.425	0.070	0.175	0.400	0.850	2.400	334.8784	2.426E-03	301,782
133	0.425	0.070	0.225	0.400	0.850	2.400	349.3870	2.317E-03	305,822
134	0.425	0.090	0.200	0.350	0.450	1.000	343.6443	2.002E-03	573,922
135	0.450	0.110	0.250	0.400	0.450	1.400	341.1259	1.957E-03	648,482
136	0.450	0.070	0.150	0.400	0.650	1.600	340.2879	2.572E-03	229,742
137	0.450	0.090	0.150	0.300	0.850	2.200	337.3818	2.631E-03	218,382
138	0.475	0.050	0.100	0.250	0.250	1.000	336.2460	3.257E-03	106,922
139	0.475	0.090	0.150	0.300	0.450	2.200	333.6680	2.775E-03	188,042
140	0.475	0.090	0.175	0.300	0.450	1.400	332.6744	2.564E-03	252,262
141	0.500	0.150	0.200	0.400	0.450	2.200	329.5684	2.230E-03	442,202
142	0.500	0.150	0.200	0.400	0.650	2.400	332.8651	2.216E-03	436,082
143	0.500	0.090	0.250	0.400	1.050	2.400	322.1735	2.785E-03	210,182

Table A2
Undercut models with fatigue crack initiation life at 150 MPa, 172 MPa, and 200 MPa stress ranges.

	Undercut Geometry						150 MPa Stress Range			172 MPa Stress Range			200 MPa Stress Range		
SN	d [mm]	r [mm]	w_L [mm]	w [mm]	l_L [mm]	l [mm]	σ_{max} [MPa]	ε_a	N_i	σ_{max} [MPa]	ε_a	N_i	σ_{max} [MPa]	ε_a	N_i
1	0.130	0.100	0.150	0.320	0.550	1.100	339.63	1.148E-03	7,377,642	340.29	1.313E-03	3,827,682	336.06	1.626E-03	1,516,562
2	0.130	0.060	0.150	0.460	0.250	0.900	344.42	1.199E-03	5,579,822	349.39	1.361E-03	2,856,382	347.99	1.666E-03	1,172,822
3	0.140	0.090	0.200	0.500	0.400	1.800	340.64	1.225E-03	5,297,462	341.98	1.429E-03	2,517,022	340.75	1.749E-03	1,040,462
4	0.150	0.110	0.150	0.400	0.250	0.800	327.12	1.113E-03	10,384,662	338.09	1.268E-03	4,657,662	335.18	1.535E-03	1,988,322
5	0.170	0.090	0.200	0.540	0.800	2.700	342.72	1.280E-03	4,171,242	342.11	1.527E-03	1,853,162	345.06	1.866E-03	751,402
6	0.190	0.050	0.200	0.340	1.850	3.800	363.13	1.755E-03	785,502	373.30	2.128E-03	328,182	388.31	2.531E-03	153,082
7	0.200	0.130	0.200	0.400	1.050	2.400	338.08	1.262E-03	4,754,542	335.64	1.484E-03	2,303,462	337.56	1.812E-03	933,042
8	0.220	0.070	0.200	0.360	1.050	2.500	351.06	1.635E-03	1,224,602	357.59	1.979E-03	512,762	376.84	2.421E-03	198,122
9	0.240	0.050	0.100	0.440	1.250	3.200	368.96	1.947E-03	483,542	383.41	2.342E-03	209,602	408.17	2.848E-03	88,362
10	0.270	0.100	0.350	0.560	1.250	3.200	342.36	1.431E-03	2,485,302	340.52	1.719E-03	1,125,802	353.05	2.099E-03	428,262
11	0.280	0.110	0.250	0.400	0.950	2.400	340.33	1.488E-03	2,136,062	341.21	1.785E-03	948,422	355.87	2.175E-03	361,722
12	0.300	0.050	0.250	0.350	0.450	2.000	362.47	1.939E-03	527,502	378.11	2.341E-03	220,742	403.28	2.840E-03	92,622
13	0.300	0.090	0.150	0.460	0.750	3.200	347.42	1.748E-03	961,922	357.26	2.088E-03	416,822	377.82	2.535E-03	167,382
14	0.350	0.110	0.250	0.560	1.300	3.800	336.31	1.574E-03	1,750,942	341.25	1.881E-03	762,462	358.34	2.280E-03	295,242
15	0.350	0.060	0.150	0.300	0.750	2.200	375.38	2.157E-03	305,242	394.76	2.591E-03	133,842	423.15	3.157E-03	57,802
16	0.400	0.050	0.150	0.300	0.850	1.800	386.22	2.251E-03	235,222	406.23	2.707E-03	105,462	428.52	3.258E-03	50,782

Appendix B

The geometric parameters of the undercut were combined to form different undercut variables to represent the 3D undercut geometry, and their fitting to the logarithmic fatigue crack initiation life was examined. The R-squared values for linear fit is presented in Table B1, along with the p-value from ANOVA test. The parameters with p-value < 0.05 are considered statistically significant parameters.

Table B1
Examples of few tested undercut geometry combinations for the 3D undercut geometry indicator.

Undercut Geometry Combinations	ANOVA p value	R squared	P value (linear fit)
$\log\left(\left(\frac{d}{r}\right)^2\left(\frac{l}{w}\right)\right)$	0.000214942	0.945721	4.27E-91
$\log\left(\left(\frac{d}{r}\right)^2 l\right)$	0.000116657	0.88667	1.53E-68
$\log(d/r)$	2.67E-17	0.868516	5.46E-64
d/r	2.97E-17	0.791002	8.85E-50
$\left(\frac{d}{r}\right)^2\left(\frac{l}{w}\right)$	0.000610016	0.681599	7.38E-37
$\left(\frac{d}{r}\right)^2\left(\frac{l}{w}\right)\sqrt{1-asym}$	0.006890915	0.667336	1.64E-35
$\frac{d}{r}\frac{l}{w}\sqrt{\left(\frac{w_L}{w}\right)^2+\left(\frac{l_L}{l}\right)^2}$	0	0.654845	2.22E-34
$\frac{d}{r}\frac{l}{w}\sqrt{1-asym}$	0.006890915	0.649357	6.79E-34
$\left(\frac{d}{r}\right)^2 l$	0.000116657	0.64022	4.19E-33
Undercut Opening Angle (β)	0.000107998	0.481891	7.06E-22
$\sqrt{d}$	1.73E-09	0.447933	6.42E-20
$\log(r)$	4.98E-12	0.41473	4.09E-18
r^2	4.98E-12	0.33654	3.13E-14
d/β	0.000107998	0.321052	1.63E-13
$d.l$	0.000444803	0.296893	1.99E-12
$UndercutArea_{length}$	0.000444803	0.296893	1.99E-12
$\log(w/l)$	0.006564967	0.241198	4.74E-10
w/l	0.008604568	0.232953	1.03E-09
d/l	0.30404957	0.105675	7.45E-05
$UndercutArea_{width}$	0.000798601	0.094527	0.000188
Undercut Volume	0.275818418	0.070719	0.001327
$(1-asym)$	0.493035608	0.017403	0.116282

References

[1] Radaj D, Sonsino CM, Fricke W. 5 - Notch strain approach for seam-welded joints. In: Radaj D, Sonsino CM, Fricke W, editors. Fatigue Assessment of Welded Joints by Local Approaches (Second Edition). Second Edition, Woodhead Publishing; 2006, p. 191–232. Doi: 10.1533/9781845691882.191.

[2] Schork B, Kucharczyk P, Madia M, Zerbst U, Hensel J, Bernhard J, et al. The effect of the local and global weld geometry as well as material defects on crack initiation and fatigue strength. Eng Fract Mech 2018;198:103–22. https://doi.org/10.1016/j.engfracmech.2017.07.001.

[3] Niraula A, Remes H, Lehto P. Local weld geometry-based characterization of fatigue strength in laser-MAG hybrid welded joints. Welding in the World 2023;67:1527–44. https://doi.org/10.1007/s40194-023-01488-5.

[4] Volvo Group. STD 181-0004 Smältsvetsning Volvo Group 2017.

[5] ISO 5817:2014. Welding — Fusion-welded joints in steel , nickel , titanium and their alloys (beam welding excluded) — Quality levels for imperfections. European Committee for Standardization 2014:38.
[6] Jonsson B, Dobmann G, Hobbacher AF, Kassner M, Marquis G. IIW Guidelines on Weld Quality in Relationship to Fatigue Strength. Cham: Springer International Publishing; 2016. Doi: 10.1007/978-3-319-19198-0.
[7] ISO 12932:2013. Welding — Laser-arc hybrid welding of steels, nickel and nickel alloys — Quality levels for imperfections. 2013.
[8] Frostevarg J, Kaplan AFH. Undercuts in Laser Arc Hybrid Welding. Phys Procedia 2014;56:663–72. https://doi.org/10.1016/J.PHPRO.2014.08.071.
[9] ISO 13847:2013. Petroleum and natural gas industries — Pipeline transportation systems — Welding of pipelines. ISO 2013. https://www.iso.org/standard/45120.html (accessed December 13, 2023).
[10] Remes H, Gallo P, Jelovica J, Romanoff J, Lehto P. Fatigue strength modelling of high-performing welded joints. Int J Fatigue 2020;135:105555. https://doi.org/10.1016/j.ijfatigue.2020.105555.
[11] Smith RA, Miller KJ. Prediction of fatigue regimes in notched components. Int J Mech Sci 1978;20:201–6. https://doi.org/10.1016/0020-7403(78)90082-6.
[12] Heinz N. Theory of notch stresses: Principles for exact calculation of strength with reference to structural form and material. 2nd ed. Tennessee: Oak Ridge; 1961.
[13] Schubnell J, Jung M, Le CH, Farajian M, Braun M, Ehlers S, et al. Influence of the optical measurement technique and evaluation approach on the determination of local weld geometry parameters for different weld types. Welding in the World 2020;64:301–16. https://doi.org/10.1007/s40194-019-00830-0.
[14] Jung M, Braun M, Schubnell J, Remes H. Round robin study on the determination of weld geometry parameters - Part A: Analysis of a reference specimen. IIW Document XIII-2993-2023 2023.
[15] Wu D, Van Nguyen A, Tashiro S, Hua X, Tanaka M. Elucidation of the weld pool convection and keyhole formation mechanism in the keyhole plasma arc welding. Int J Heat Mass Transf 2019;131:920–31. https://doi.org/10.1016/J.IJHEATMASSTRANSFER.2018.11.108.
[16] Fabbro R, Frederic C, Briand F, Liquide A. Experimental study of the humping process during Nd:YAG laser welding 2007.
[17] Bell R, Vosikovsky O, Bain S. The significance of weld toe undercuts in the fatigue of steel plate T-joints. Int J Fatigue 1989;11:3–11. https://doi.org/10.1016/0142-1123(89)90041-8.
[18] Iida K, Miyasako K, Ohgi M, Okano Y. an investigation of influencing factors on bending fatigue strength of fillet welded joint. J Soc Naval Arch Japan 1978;1978:434–45. https://doi.org/10.2534/jjasnaoe1968.1978.434.
[19] Petershagen H. The influence of undercut on the fatigue strength of welds: a literature survey. Welding in the World 1990;28:114–25.
[20] Hultgren G, Barsoum Z. Fatigue assessment in welded joints based on geometrical variations measured by laser scanning. Welding in the World 2020;64:1825–31. https://doi.org/10.1007/s40194-020-00962-8.
[21] Niederwanger A, Ladinek M, Lener G. Strain-life fatigue assessment of scanned weld geometries considering notch effects. Eng Struct 2019;201:109774. https://doi.org/10.1016/j.engstruct.2019.109774.
[22] Ottersböck MJ, Leitner M, Stoschka M. Characterisation of actual weld geometry and stress concentration of butt welds exhibiting local undercuts. Eng Struct 2021;240:1–13. https://doi.org/10.1016/j.engstruct.2021.112266.
[23] Cerit M, Kokumer O, Genel K. Stress concentration effects of undercut defect and reinforcement metal in butt welded joint. Eng Fail Anal 2010;17:571–8. https://doi.org/10.1016/j.engfailanal.2009.10.010.
[24] Nguyen NT, Wahab MA. The effect of undercut, misalignment and residual stresses on the fatigue behaviour of butt welded joints. Fatigue Fract Eng Mater Struct 1996;19:769–78. https://doi.org/10.1111/j.1460-2695.1996.tb01321.x.
[25] Nguyen NT, Wahab MA. The effect of undercut and residual stresses on fatigue behaviour of misaligned butt joints. Eng Fract Mech 1996;55:453–69. https://doi.org/10.1016/0013-7944(96)00024-0.
[26] Mashiri FR, Zhao XL, Grundy P. Effects of weld profile and undercut on fatigue crack propagation life of thin-walled cruciform joint. Thin-Walled Struct 2001;39:261–85. https://doi.org/10.1016/S0263-8231(00)00061-6.
[27] Jubb JEM. Undercut or toe groove-the Cinderella defect. Metal. Construction 1981;94.
[28] Wahab MA, Alam MS. The significance of weld imperfections and surface peening on fatigue crack propagation life of butt-welded joints. J Mater Process Technol 2004;153–154:931–7. https://doi.org/10.1016/j.jmatprotec.2004.04.150.
[29] Niederwanger A, Warner DH, Lener G. The utility of laser scanning welds for improving fatigue assessment. Int J Fatigue 2020;140:105810. https://doi.org/10.1016/j.ijfatigue.2020.105810.
[30] Liinalampi S, Remes H, Romanoff J. Influence of three-dimensional weld undercut geometry on fatigue-effective stress. Welding in the World 2019;63:277–91. https://doi.org/10.1007/s40194-018-0658-7.
[31] Hartloper AR, de Castro e Sousa A, Lignos DG. Constitutive Modeling of Structural Steels: Nonlinear Isotropic/Kinematic Hardening Material Model and Its Calibration. J Struct Eng 2021;147. https://doi.org/10.1061/(ASCE)ST.1943-541X.0002964.
[32] Remes H. Strain-based approach to fatigue crack initiation and propagation in welded steel joints with arbitrary notch shape. Int J Fatigue 2013;52:114–23. https://doi.org/10.1016/j.ijfatigue.2013.03.006.
[33] Lehto P, Remes H. EBSD characterisation of grain size distribution and grain substructures for ferritic steel weld metals. Welding in the World 2022;66:363–77. https://doi.org/10.1007/s40194-021-01225-w.
[34] CSC – IT Center for Science. High Performance Computing - Services for Research - CSC Company Site 2023. https://research.csc.fi/csc-s-servers (accessed December 20, 2023).
[35] Garcia MAR. Multiaxial fatigue analysis of high-strength steel welded joints using generalized local approaches. 2020. Doi: 10.5075/EPFL-THESIS-7394.
[36] Roessle M, Fatemi A. Strain-controlled fatigue properties of steels and some simple approximations. Int J Fatigue 2000;22:495–511. https://doi.org/10.1016/S0142-1123(00)00026-8.
[37] Remes H. Strain-Based Approach to Fatigue Strength Assessment of Laser-Welded Joints. Espoo: TKK Dissertations 102; 2008.
[38] Dowling N, Siva Prasad K, Narayanasamy R. Mechanical Behavior of Materials. Mechanical Behavior of Materials. 4th ed.,. Boston: Pearson; 2013. p. 417.
[39] Nguyen TN, Wahab MA. The effect of weld geometry and residual stresses on the fatigue of welded joints under combined loading. J Mater Process Technol 1998;77:201–8. https://doi.org/10.1016/S0924-0136(97)00418-4.
[40] Gosch T, Petershagen H. Influence of undercuts on the fatigue strength of butt welds. Schweissen Und Schneiden 1997;49(3):E44–6.
[41] Janosch JJ, Debiez S. Influence of the shape of undercut on the fatigue strength of fillet welded assemblies - application of the local approach. Welding in The World 1998;41:350–60.
[42] Wei G, Hu K, Chen S, Yan M. Experiment and simulation investigation of multiple cracks evolution at the weld toe. Int J Fatigue 2021;144. https://doi.org/10.1016/j.ijfatigue.2020.106037.
[43] Baumgartner J. Review and considerations on the fatigue assessment of welded joints using reference radii. Int J Fatigue 2017;101:459–68. https://doi.org/10.1016/j.ijfatigue.2017.01.013.
[44] Dong Y, Garbatov Y, Guedes SC. A two-phase approach to estimate fatigue crack initiation and propagation lives of notched structural components. Int J Fatigue 2018;116:523–34. https://doi.org/10.1016/J.IJFATIGUE.2018.06.049.